Available online at www.sciencedirect.com
ScienceDirect
Comput. Methods Appl. Mech. Engrg. 331 (2018) 232–258
Computer methods in applied mechanics and engineering
www.elsevier.com/locate/cma

Laser-induced heating of dynamic particulate depositions in additive manufacturing

T.I. Zohdi

Department of Mechanical Engineering, 6117 Etcheverry Hall, University of California, Berkeley, CA, 94720-1740, USA

Received 3 August 2017; received in revised form 29 October 2017; accepted 2 November 2017
Available online 15 November 2017

Abstract

Many applications in additive manufacturing involve the dynamic deposition of powders and the in-flight heating of such material by a laser. In order to characterize such systems, the Discrete Element Method (DEM) is employed. Specifically, this paper focuses on the initial stages of this process by developing a modular discrete-element type multiphysics simulation method for the particle dynamics and heating by a laser and detailed thermal behavior. The objective is to provide researchers with a framework to construct computational tools for this growing industry. In order to achieve this, from a simulation standpoint, the overall particle-mixture system is constructed by coupling submodels for each primary physical process (dynamics and heating) together. An iterative staggering scheme is developed whereby, within every time step, each individual particle is solved "freezing" the state of the remaining multiparticle system. The state of the particle is then updated and the algorithm moves to the next particle in the system and the process is repeated. The overall process sweeps through the entire system repeatedly until convergence is achieved in an appropriate norm. As the system evolves, an error estimate dictates the time-step size that is needed to induce convergence to below an appropriate error level. Thus, the process can be considered as an implicit time-stepping scheme, which is combined with an (internal) iterative staggering process. In order to control rates of convergence within a time-step, the algorithm adjusts the time-step size. If the iterative process does not converge within a desired number of iterations, below an error tolerance, the time-step is reduced. The degree of time-step reduction is determined by utilizing an estimate of the spectral radius of the coupled system. Since the construction of model and solution process is modular, one can easily replace physical submodels with other choices, making it easy to numerically experiment with a variety of models. Qualitative and quantitative analyses are provided, as well as three-dimensional numerical examples. This paper addresses the first of two overall "macrostages" of a complex manufacturing process with DEM. The first stage, addressed in this paper, concentrates on dry-powder materials, which are of a discrete particulate character, using DEM to characterize the deposition and in-flight particle heating. Other papers of the author (Zohdi, 2010, 2013, 2014, 2015 [81,82], 2008) have addressed stage two, namely phase transformations, curing (cooling) and stress analysis, using more appropriate continuum and hybrid DEM-continuum approaches.

Keywords: Particles; Dynamic deposition; Laser; Heating

E-mail address: zohdi@berkeley.edu.

https://doi.org/10.1016/j.cma.2017.11.003
0045-7825/

1. Introduction

A large variety of emerging advanced fabrication methods involve Additive Manufacturing (AM) processes, which are generally characterized as depositing materials onto substrates and bonding them together to create structures, as opposed to classical "subtractive" processes which remove material. The approach was pioneered in 1984 by Hull [1] and was a 2.9 billion dollar industry in 2015, with applications ranging from motor vehicles, consumer products, medical devices, military hardware and the arts. We refer readers to a recent review of the state of the art by Huang et al. [2]. A subclass of AM processes involve "dry" powder deposition. "Dry" powder deposition approaches (where the interstitial space between particles is not saturated with a liquid) do not utilize solvents, since the deposited material will be heated or cured afterwards in order to harden it into place. Interstitial solvents are avoided because they can compromise the resulting hardened material quality, due to gas bubbles, mass-transport induced cracking, etc., during curing. *However, the precise deposition of dry powders is difficult.* It is for this reason, electrically-driven methods are being pursued, whereby the dry particles are ionized and an electric field is used to guide them into place. A key aspect of these processes are the precise deposition of specialized mixtures of materials. The design of the deposited material properties is enabled by the use of added particles to endow the correct functionality ("functionalization") to the material (Fig. 1).

In many cases, these materials are specially designed mixtures of "dry" powders (particles), whereby one set of particles is chosen with the objective to electrically, thermally or mechanically functionalize the overall material and another set of finer-scale particles serves as an interstitial filler/binder. The rapid rise in the use of particle-based materials has been made possible by the large-scale production of consistent, high-quality and inexpensive particles, which are manufactured in many ways, such as breakup of liquid streams into solidified droplets or vaporization from a solid or liquid to a gas and recapturing the condensate in the form of particles. In addition to electrical control, an increasingly large number of advanced additive manufacturing processes involve the deposition of particles followed by a laser to thermally-process the particles. Because of the large number of system parameters in these multistage processes, modeling and simulation have become key components in ascertaining the proper combinations to achieve desired results. The objective of this paper is to develop models for this type of process.

As mentioned, achieving precisely controlled deposition of such dry particulate-based materials is difficult or impossible by solely mechanical means. It is for this reason, electrically-driven methods are being pursued in industry, whereby the particles are ionized and an electric field is used to guide them into place (Fig. 1). The goal of this work is to develop a model and simulation method to investigate the behavior of such depositions as a function of the applied electric field. There is a direct correlation between the ionization strength between particles in the powder and the more fluid-like behavior. Effectively, with no ionization, the system behaves as a loose powder, which is difficult to control. As the ionization is ramped up, the balance between mutual attraction and repulsion leads to surface tension like effects. Thus, the expectation is that at high external fields and high ionization, the deposition will yield coherent aggregate "droplets" of the powder-mixture material.

Dry powders require nonstandard modeling and simulation tools to characterize their behavior as compared to continua. numerical approaches designed for continuum simulation (such as Finite Element Methods) are not well-suited to describe the dynamics of discrete particles, with overall domains that break apart, coalesce or experience other extremely large configurational changes. One family of methods that is ideally suited to this task are Discrete Element Methods (DEM), which is the approach pursued in this paper.[1] In order for new *additive approaches to succeed, such as the one mentioned, one must utilize theory and computation to guide the proper selection of particle mixtures to progress to robust large-scale industrial manufacturing levels.* Due to increasingly shorter product development times in the additive manufacturing field, there is a critical need for simulation tools. This has motivated the analysis in this paper, which attempts to develop a DEM computational framework which captures the dynamics of particle-to-particle and particle-to-substrate interaction under the influence of electric fields. As previously mentioned, to enhance control of depositions, the deposited particles are ionized and guided to the surface with an electromagnetic field. Ionization can be achieved through a variety of possible methods, such as by passing the particles through a charged gas or applying an electrified surfactant. We refer the reader to Martin [53,54], Choi et al. [55–58] and Demko et al. [59] for overviews of the various related processes. Generally speaking, this process is physically quite similar to methods used in spray coating technologies (see Martin [53,54] for the state of the art, as well as Sevostianov and

[1] For details, see Duran [3], Pöschel and Schwager [4], Oñate et al. [5–7], Rojek et al. [8,9], Carbonell et al. [10], Labra and Oñate [11], Mukherjee et al. [12–15] and Zohdi [16–52].

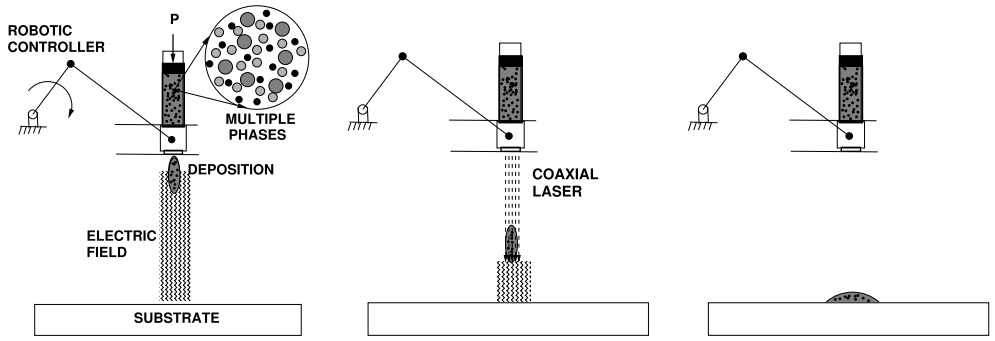

Fig. 1. A schematic of a multistage process.

Kachanov [60–62], Qian et al. [63], Dwivedi et al. [64], Liu et al. [65,66], Nakamura and Liu [67] and Nakamura et al. [68]). Oftentimes, these types of materials are used to lay down electronic lines or patterns on compliant substrates, such as flexible, "smart", electronics, such as high-end solar cells. We refer the reader to the literature on printed electronics field found in Gamota [69], Nakanishi et al. [70], Fuller et al. [71], Samarasinghe et al. [72], Ahmad et al. [73], Sirringhaus et al. [74], Wang et al. [75], Huang et al. [76], Choi et al. [55–58] and Demko et al. [59,77] for details.

Remark. It is important to note that this paper addresses the first of two overall "macrostages" of a complex manufacturing process with DEM. In the first stage, addressed in this paper, dry-powder materials, which are of a discrete particulate character, are modeled using DEM for the deposition and in-flight heating phase of the process. Other papers of the author (Zohdi [78–83]) have addressed stage two, namely phase transformations, curing (cooling) and stress analysis, using more appropriate continuum and hybrid DEM-continuum approaches.

2. Qualitative behavior

2.1. Qualitative electrodynamics

Consider the governing equation for a deposited particle:

$$m\dot{\boldsymbol{v}} = q\boldsymbol{E}^{ext} + m\boldsymbol{g}, \tag{2.1}$$

where the applied external electric field is $\boldsymbol{E}^{ext}$ and $\boldsymbol{g}$ is the gravitational field. Integrating, with initial conditions $\boldsymbol{r}(t=0) = \boldsymbol{r}_o$ and $\boldsymbol{v}(t=0) = \boldsymbol{v}_o$

$$\boldsymbol{r}(t) = \left(\frac{q\boldsymbol{E}^{ext}}{m} + \boldsymbol{g}\right)\frac{t^2}{2} + \boldsymbol{v}_o t + \boldsymbol{r}_o. \tag{2.2}$$

The travel distance is

$$\boldsymbol{r}_o - \boldsymbol{r}(t) = -\left(\frac{q\boldsymbol{E}^{ext}}{m} + \boldsymbol{g}\right)\frac{t^2}{2} - \boldsymbol{v}_o t. \tag{2.3}$$

Now assuming purely vertical motion $\boldsymbol{r}(t=0) = (r_{xo}, 0, 0)$, $\boldsymbol{v}(t=0) = (-v_{xo}, 0, 0)$, $\boldsymbol{g} = (-g, 0, 0)$, $\boldsymbol{E}^{ext} = (-E_x^{ext}, 0, 0)$, leads to a quadratic equation of the form, setting $\boldsymbol{r}(t^*) = \boldsymbol{r}_x^* = (r_x^*, 0, 0)$

$$\left(\frac{qE_x^{ext}}{m} + g\right)\frac{t^2}{2} + v_{xo}t - (r_{xo} - r_x^*) = 0, \tag{2.4}$$

leading to

$$t^* = \frac{-v_{xo} + \sqrt{v_{xo}^2 + 4\left(\frac{qE_x^{ext}}{2m} + \frac{g}{2}\right)(r_{xo} - r_x^*)}}{\frac{qE_x^{ext}}{m} + g}. \tag{2.5}$$

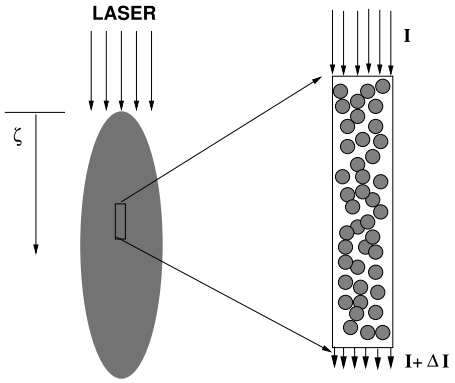

Fig. 2. Laser penetration through a material.

Remarks. The derived analytical expression (Eq. (2.5)) provides qualitative guidance for the selection of parameters:

- The larger the initial (downward) velocity, v_{xo}, the smaller the residence time,
- The larger the electric field, E_x^{ext}, the smaller the residence time,
- The larger the particle charge, q, the smaller the residence time,
- The larger the mass, m, the smaller the residence time and
- The larger the travel distance, $r_{xo} - r_x^*$, the larger the residence time.

2.2. Qualitative thermodynamics

To describe the laser heating, we utilize a Beer–Lambert framework, whereby one performs an overall power balance (Fig. 2 with $\zeta = r_{xo} - r_x$)

$$(I + \Delta I) - I + \mathcal{L}\Delta\zeta = 0 \Rightarrow \frac{dI}{d\zeta} \approx -\alpha I, \tag{2.6}$$

where $L = \alpha I$ is the absorbed irradiance (per unit area) from the laser and ζ is the penetration depth to the point in question. One can solve this differential equation to yield

$$I(\zeta) = I_o e^{-\alpha\zeta}, \tag{2.7}$$

where I_o is the irradiance at $\zeta = 0$. Using the first law of thermodynamics

$$mC\dot{\theta} = \alpha I(\zeta(t))V \tag{2.8}$$

where α is an absorption constant and $V = \frac{4}{3}\pi R^3$ is the volume of the particle. Integrating yields

$$\theta(t) = \theta_o + \int_0^t \frac{\alpha I(\zeta(t))V}{mC}\, dt. \tag{2.9}$$

In the special case that there is no attenuation/interference

$$\theta(t) = \theta_o + \frac{\alpha I_o V}{mC} t. \tag{2.10}$$

In the special case that $E_x^{ext} = 0$ and $g = 0$

$$\theta(t) = \theta_o + \frac{\alpha I_o V (r_{xo} - r_x^*)}{mC v_{xo}}. \tag{2.11}$$

If there is attenuation, then

$$\theta(t) = \theta_o + \frac{\alpha V I_o}{mC} \int_0^t e^{-\alpha\left(\left(\frac{qE_x^{ext}}{m} + g\right)\frac{t^2}{2} + v_{xo}t\right)}\, dt. \tag{2.12}$$

In the special case that $E_x^{ext} = 0$ and $g = 0$

$$\theta(t) = \theta_o + \frac{\alpha V I_o}{mC v_{xo}}(1 - e^{-\alpha(r_{xo} - r_x^*)}). \tag{2.13}$$

Taking a Taylor series in terms of $(r_{xo} - r_x^*)$ yields

$$\theta(t) = \theta_o + \frac{\alpha I_o V (r_{xo} - r_x^*)}{mC v_{xo}}. \tag{2.14}$$

and since $m = \rho V$,

$$\theta(t) = \theta_o + \frac{\alpha I_o (r_{xo} - r_x^*)}{\rho C v_{xo}}, \tag{2.15}$$

Remarks. The derived analytical expression (Eq. (2.15)) provides qualitative guidance for the selection of parameters:

- The larger the absorption constant, α, the higher the temperature,
- The larger the source irradiance, I_o, the higher the temperature,
- The larger the travel distance, $r_{xo} - r_x^*$, the higher the temperature,
- The larger the material density, ρ, the lower the temperature,
- The larger the material heat capacity, C, the lower the temperature,
- The larger the initial (downward) velocity, v_{xo}, the lower the temperature.

However, for more quantitative information, we need to resort to numerical methods that capture the multibody aspects of the deposition, which may include more physical features. Thus, while the preceding model provide qualitative guidance on the system behavior, more quantitative information requires a direct numerical simulation. In order to achieve this, from a simulation standpoint, the overall particle-mixture system is constructed by coupling submodels for each primary physical process together. An iterative staggering scheme is developed whereby, within every time step, each individual particle is solved, "freezing" the state of the remaining multi-particle system. The state of the particle is then updated and the algorithm moves to the next particle in the system and the process is repeated. The overall process sweeps through the entire system repeatedly until convergence in an appropriate norm. As the system evolves, an error estimate dictates the time-step size that is needed to induce convergence to below an appropriate error level. Essentially, this is an implicit time-stepping scheme, which is combined with an (internal) iterative staggering process. In order to control rates of convergence within a time-step, the algorithm adjusts the time-step size. If the iterative process does not converge within a desired number of iterations, below an error tolerance, the time-step is reduced. The degree of time-step reduction is determined by utilizing an estimate of the spectral radius of the coupled system. Since the construction of model and solution process is modular, one can easily replace physical submodels with other choices, making it easy to numerically experiment with a variety of models.

3. Particle dynamics

Consider a collection of N_p non-intersecting particles which are assumed to be spherical in shape. It is also assumed that the particles are small enough that their rotation with respect to their mass center minimally affects their overall motion (this is discussed further shortly). For an arbitrary ith particle in the system, acted upon by

1. $\boldsymbol{\Psi}_i^{con}$: inter-particle contact forces,
2. $\boldsymbol{\Psi}_i^{bond}$: inter-particle adhesive bonding forces,
3. $\boldsymbol{\Psi}_i^{e+m}$: inter-particle near-field and external electromagnetic forces and
4. $\boldsymbol{\Psi}_i^{drag}$: particle drag forces from any surrounding gas,

the dynamics are governed by

$$m_i \ddot{\boldsymbol{r}}_i = \boldsymbol{\Psi}_i^{con} + \boldsymbol{\Psi}_i^{bond} + \boldsymbol{\Psi}_i^{e+m} + \boldsymbol{\Psi}_i^{drag} \stackrel{\text{def}}{=} \boldsymbol{\Psi}_i^{tot}(\boldsymbol{r}_1, \boldsymbol{r}_2, \ldots, \boldsymbol{r}_{N_p}), \tag{3.1}$$

where $\boldsymbol{r}_i$ is the position vector of the ith particle and $\boldsymbol{\Psi}_i^{tot}$ is the total of the forces acting on the ith particle. The various types of force categories will now be explained further.

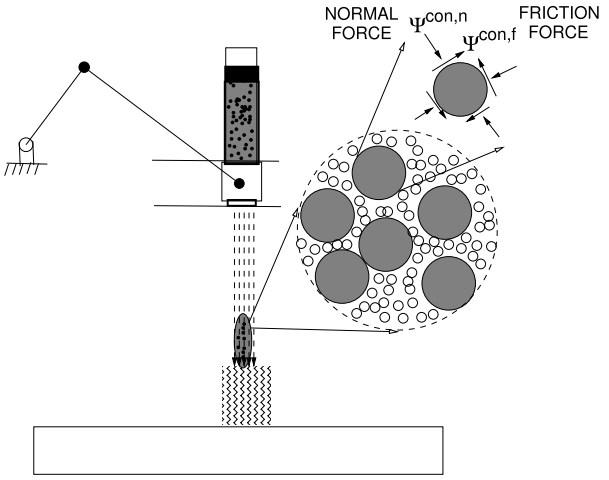

Fig. 3. Contact, decomposed into normal and tangential friction forces.

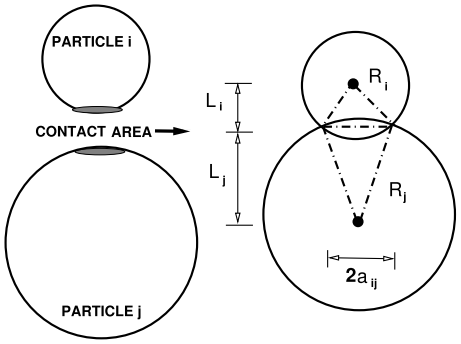

Fig. 4. A contact area parameter for two particles.

3.1. Particle contact forces

A straightforward "overlap" model (Zohdi [12–52,55–58,60–62,79–117]) is used to determine the normal contact forces between particles. Consider the ith particle in contact with N_{ci} particles, producing a total contact force of $\boldsymbol{\Psi}_i^{con,n} = \sum_{j=1}^{N_{ci}} \boldsymbol{\psi}_{ij}^{con,n}$, where the forces are dictated by the separation distance between the particle centers for the particle in contact (Fig. 3), written generally as

$$\boldsymbol{\Psi}_{ij}^{con,n} = \mathcal{F}(\|\boldsymbol{r}_i - \boldsymbol{r}_j\|, R_i, R_j, material\ properties), \tag{3.2}$$

where R_i and R_j are the radii of the ith and jth particles in contact. In the literature, there is a large number of contact models for normal force generation. For simplicity, we assume that the contact force is proportional to the distance between the centers of particles i and j (when in contact). Contact is determined by checking if $\|\boldsymbol{r}_i - \boldsymbol{r}_j\| \leq R_i + R_j$. We construct an overlap function, $\delta_{ij} \stackrel{\text{def}}{=} |\|\boldsymbol{r}_i - \boldsymbol{r}_j\| - (R_i + R_j)|$, and a corresponding normal contact force[2]

$$\boldsymbol{\Psi}_{ij}^{con,c} \propto -K_{pij} |\mathcal{E}_{ij}|^{p_p} \boldsymbol{n}_{ij} A_{ij}^c, \tag{3.3}$$

[2] A_{ij}^c is a contact area parameter (Fig. 4) discussed in Appendix A, along with a review of classical Hertzian and other models.

where $0 < K_{pij} < \infty$ is a contact constant, p_p is a material parameter and $\mathcal{E}_{ij}$ is nondimensional strain-like deformation metric

$$\mathcal{E}_{ij} = |\frac{\|\boldsymbol{r}_i - \boldsymbol{r}_j\| - (R_i + R_j)}{(R_i + R_j)}| = \frac{\delta_{ij}}{(R_i + R_j)} \tag{3.4}$$

and $\boldsymbol{n}_{ij} = -\frac{\boldsymbol{r}_i - \boldsymbol{r}_j}{\|\boldsymbol{r}_i - \boldsymbol{r}_j\|} = \frac{\boldsymbol{r}_j - \boldsymbol{r}_i}{\|\boldsymbol{r}_i - \boldsymbol{r}_j\|}$.

3.1.1. Rotations

Including particle rotations is questionable for extremely small objects (idealized as spherical particles), since in reality they are not perfectly spherical (even if they are manufactured to be as close to spherical as possible) and, importantly, because of rolling resistance. However, for completeness, we illustrate the inclusion of rotational equations of motion (a balance of angular momentum), which augment a balance of linear momentum, $m_i \dot{\boldsymbol{v}}_i = \boldsymbol{\Psi}_i^{tot}$, $\boldsymbol{v}_i$ being the center of mass velocity. The balance of angular momentum reads

$$\dot{\boldsymbol{H}}_{i,\,cm} = \frac{d(\bar{\boldsymbol{I}}_i \cdot \boldsymbol{\omega}_i)}{dt} = \boldsymbol{M}_{i,\,cm}^{tot}, \tag{3.5}$$

where, for spheres, we have $\boldsymbol{H}_{i,\,cm} = \bar{I}_{i,s}\boldsymbol{\omega}_i = \frac{2}{5} m_i R_i^2 \boldsymbol{\omega}_i$. The total moment, $\boldsymbol{M}_{i,\,cm}^{tot}$, is due to interaction forces, contact forces and rolling resistance. In the present analysis, the effects of rotations are generally negligibly small. Regardless, we will formulate the system with rotations, where the important dynamical states of each particle are the $\boldsymbol{r}_i$ is the position and $\boldsymbol{v}_i$ is the velocity of the center of mass and $\boldsymbol{\omega}_i$ is the angular velocity. A critical variable of interest is the velocity on the surface of the "particles" at contact points (with other particles), denoted $\boldsymbol{v}_i^c$ and is computed by $\boldsymbol{v}_i^c = \boldsymbol{v}_i + \boldsymbol{\omega}_i \times \boldsymbol{r}_{i\rightarrow c}$, where the relative position vector from the center of mass to the possible point of contact is given by $\boldsymbol{r}_{i\rightarrow c}$. This is utilized further later in the formulation.[3]

3.1.2. Dissipation during contact

One can incorporate phenomenological descriptions of contact dissipation by tracking the relative velocity of the contacting particles by simply including

$$\boldsymbol{\Psi}_{ij}^{con,d} = c^{cd}(\boldsymbol{v}_{j,n} - \boldsymbol{v}_{i,n})A_{ij}^c, \tag{3.7}$$

where c^{cd} is a contact dissipation parameter.

3.1.3. Contact induced friction

At the point of contact, "sticking" induced by friction is captured via the following "regularized" friction algorithm:

1. First one checks the threshold limit for static friction:

$$K^f \|\boldsymbol{v}_{j,\tau}^c - \boldsymbol{v}_{i,\tau}^c\| A_{ij}^c \Delta t \text{ against } \mu_s \|\boldsymbol{\Psi}^{con,n}\|, \tag{3.8}$$

   where K^f is a tangential contact friction compliance constant, $\|\boldsymbol{v}_{j,\tau}^c - \boldsymbol{v}_{i,\tau}^c\|\Delta t$ is the relative tangential velocity at (the point of contact), Δt is the time-step used in the numerical discretization,[4] μ_s is the static friction coefficient. *This step "regularizes" (replaces) a potentially more difficult process of initially assuming no slip, then calculating the no-slip contact forces by solving an entire multibody/multisurface contact problem, $\boldsymbol{\Psi}^{ns}$, then thereafter checking Ψ^{ns} against the static friction limit $\mu_s \|\boldsymbol{\Psi}^{con,n}\|$ on each surface.*
2. Second, if the threshold limit is not met, namely $K^f \|\boldsymbol{v}_{j,\tau}^c - \boldsymbol{v}_{i,\tau}^c\| A_{ij}^c \Delta t < \mu_s \|\boldsymbol{\Psi}^{con,n}\|$, then one computes

$$\boldsymbol{\Psi}^{con,f} = K^f \|\boldsymbol{v}_{j,\tau}^c - \boldsymbol{v}_{i,\tau}^c\| A_{ij}^c \Delta t \boldsymbol{\tau}_{ij}^c \tag{3.9}$$

[3] Consequently, an implicit time discretization reads

$$\boldsymbol{\omega}_i(t + \Delta t) = \boldsymbol{\omega}_i(t) + \frac{\Delta t}{\bar{I}_{i,s}} \left(\phi \boldsymbol{M}_{i,\,cm}^{tot}(t + \Delta t) + (1 - \phi)\boldsymbol{M}_{i,\,cm}^{tot}(t)\right), \tag{3.6}$$

which is discussed further later.

[4] Note $\|\boldsymbol{v}_{j,\tau}^c - \boldsymbol{v}_{i,\tau}^c\|\Delta t$ has dimensions of length.

where (here the subscripts denote the tangential components of velocity)

$$\boldsymbol{\tau}_{ij}^{c} = -\frac{\boldsymbol{v}_{i,\tau}^{c} - \boldsymbol{v}_{j,\tau}^{c}}{\|\boldsymbol{v}_{j,\tau}^{c} - \boldsymbol{v}_{i,\tau}^{c}\|} = \frac{\boldsymbol{v}_{j,\tau}^{c} - \boldsymbol{v}_{i,\tau}^{c}}{\|\boldsymbol{v}_{j,\tau}^{c} - \boldsymbol{v}_{i,\tau}^{c}\|}, \tag{3.10}$$

where subtracting away the normal component of the velocity $\boldsymbol{v}_t^c = \boldsymbol{v}^c - (\boldsymbol{v}^c \cdot \boldsymbol{n})\boldsymbol{n}$ yields the contact point's tangential velocity.

3. Third, if the threshold limit is met (or exceeded), specifically $K^f \|\boldsymbol{v}_{j,\tau}^{c} - \boldsymbol{v}_{i,\tau}^{c}\| A_{ij}^{c} \Delta t \geq \mu_s \| \boldsymbol{\Psi}^{con,n} \|$, then one employs a slip model

$$\boldsymbol{\Psi}_{ij}^{con,f} = \mu_d \| \boldsymbol{\Psi}_{ij}^{con,n} \| \boldsymbol{\tau}_{ij}^{c}, \tag{3.11}$$

where μ_d is the dynamic coefficient of friction.

3.2. Particle-to-particle bonding relations

As a criterion for particles to bond, we adopt a threshold dictated by exceeding a critical interpenetration distance, computed in the following manner:

1. First, recall that if $\|\boldsymbol{r}_i - \boldsymbol{r}_j\| \leq (R_i + R_j)$, then the particles are in contact and $\mathcal{E}_{ij} = \frac{\delta_{ij}}{(R_i + R_j)}$.
2. Second, for particles in contact, $|\mathcal{E}_{ij}| \geq \mathcal{E}^*$, an adhesive/attractive normal bond ($0 \leq K_{ij}^{nb}$) is activated between the particles is a bonding constant and p_b is a material parameter :

$$\boldsymbol{\Psi}_{ij}^{bond,n} = K_{ij}^{nb} |\mathcal{E}_{ij}|^{p_b} \boldsymbol{n}_{ij} A_{ij}^{c}. \tag{3.12}$$

3. Third, for particles with an activated normal bond, the particles automatically have an activated rotational/tangential bond (similar in form to stick friction)[5]

$$\boldsymbol{\Psi}_{ij}^{bond,r} = K_{ij}^{rb} \|\boldsymbol{v}_{j,\tau}^{c} - \boldsymbol{v}_{i,\tau}^{c}\| A_{ij}^{c} \Delta t \boldsymbol{\tau}_{ij}^{c}, \tag{3.13}$$

as well as a torsional bond of the form

$$\boldsymbol{M}_{ij}^{bond,t} = K_{ij}^{rt} \left((\boldsymbol{\omega}_i - \boldsymbol{\omega}_j) a^2 \cdot \boldsymbol{n} \right) A_{ij}^{c} \Delta t \boldsymbol{n}, \tag{3.14}$$

where a is the contact area radius (see Appendix A–C). The same model is also used for torsional frictional moments.

Note: We assume that torsional friction is due to relative spinning along axis connecting the particle centers. The effect is generally small, unless the particles are bonded to one another.

3.3. Near-field and electromagnetic forces

We decompose the electromagnetic forces into three parts: (1) Lorentz forces (for charged particles), (2) inter-particle near-field forces and (3) magnetic forces (for magnetic particles). In mathematical form,

$$\boldsymbol{\Psi}_i^{e+m} = \boldsymbol{\Psi}_i^{lor,e+m} + \boldsymbol{\Psi}_i^{mag} + \underbrace{\sum_{j \neq i}^{N} \boldsymbol{\psi}_{ij}^{nf}}_{\boldsymbol{\Psi}_i^{nf}} = \underbrace{q_i(\boldsymbol{E}^{ext} + \boldsymbol{v}_i \times \boldsymbol{B}^{ext})}_{\boldsymbol{\Psi}_i^{lor,e+m}} + \boldsymbol{\Psi}_i^{nf} + \boldsymbol{\Psi}_i^{mag}, \tag{3.15}$$

where the interaction between particle i and all other particles $j = 1, 2, 3, \ldots, N$ ($j \neq i$), is $\sum_{j \neq i}^{N} \boldsymbol{\psi}_{ij}^{nf}$ and the applied Lorentz-induced forces from independent external fields $\boldsymbol{E}^{ext}$ and $\boldsymbol{B}^{ext}$ is $\boldsymbol{\Psi}_i^{lor,e+m}$. The terms $\boldsymbol{E}^{ext}$ and $\boldsymbol{B}^{ext}$ are considered to be externally controlled and uncoupled from one another.[6]

[5] Selections for the values of the parameters in these models are given later in the presentation.

[6] For the velocity ranges in the present applications (significantly below the speed of light), self-induced magnetic fields between particles are unimportant (Jackson [84]).

Following Zohdi [80,85–90], a simple form that captures the essential near-field effects is

$$\boldsymbol{\Psi}_i^{nf} = \sum_{j \neq i}^{N_p} \left(\underbrace{\alpha_{1ij} \|\boldsymbol{r}_i - \boldsymbol{r}_j\|^{-\beta_1}}_{\text{attraction}} - \underbrace{\alpha_{2ij} \|\boldsymbol{r}_i - \boldsymbol{r}_j\|^{-\beta_2}}_{\text{repulsion}} \right) \boldsymbol{n}_{ij}, \tag{3.16}$$

where the α's and β's are empirical material parameters. Here, various representations (decompositions) of the coefficients that appear in Eq. (3.16) are with $c_i = \pm 1$ (a positive/negative multiplier):

1. charge-based: $\alpha_{ij} = \bar{\alpha}_{ij} q_i q_j c_i c_j$, where the $\bar{\alpha}_{ij}$ are empirical parameters,
2. surface area-based (a=surface area): $\alpha_{ij} = \bar{\alpha}_{ij} a_i a_j c_i c_j$,
3. volume-based (V=volume): $\alpha_{ij} = \bar{\alpha}_{ij} V_i V_j c_i c_j$ and
4. mass-based (m=mass): $\alpha_{ij} = \bar{\alpha}_{ij} m_i m_j c_i c_j$.

There exist a large number of empirical near-field relations that generally fall under the subject matter of the vast field of "Molecular Dynamics" (MD). We refer readers to Frenklach and Carmer [91], Haile [92], Hase [93], Schlick [94] and Rapaport [95], where Lennard-Jones, Mie and Morse potentials (Moelwyn-Hughes [96]) are usually employed, with various extensions such as Tersoff [97] additions and three-body terms (Stillinger [98]). For the remainder of the analysis, we neglect any possible magnetism of the particles themselves. However, we note that such forces can be described by $\boldsymbol{\Psi}^{mag} = \nabla(\gamma \boldsymbol{B}^{ext} \cdot \boldsymbol{B}^{ext})$ (independently of the Lorentz forces), where γ is a material parameter that is related to the magnetization (magnetic dipole properties, susceptibility, permeability, moment density, etc.) of the particle (see Feynman et al. [99], Cullity and Graham [100], Boyer [101] or Jackson [84]).

3.4. Drag forces

It is important to note that, ideally, one would like to eliminate a surrounding gaseous environment and run the process in a vacuum. However, this may not always be feasible, thus we include a drag term, potentially due to interstitial and surrounding gas:

$$\boldsymbol{\Psi}_i^{drag} = \frac{1}{2} \rho_g C_D \|\boldsymbol{v}^g - \boldsymbol{v}_i\| (\boldsymbol{v}^g - \boldsymbol{v}_i) A_i, \tag{3.17}$$

where C_D is the drag coefficient, A_i is the reference area, which for a sphere is $A_i = \pi R_i^2$, ρ_g is the gas density and $\boldsymbol{v}^g$ is the velocity of the surrounding gas medium. We will assume that $\boldsymbol{v}^g \approx \boldsymbol{0}$, and that the gas is of extremely low density, relative to the particles. See Appendix B for more details. We refer the reader to Zohdi [87,90] for more detailed calculations on general fluid(liquid)-particle interaction.

4. Solution strategy

With the governing equations established, we integrate Eq. (3.1) using a variable-metric ($0 \leq \phi \leq 1$) trapezoidal-like rule to obtain the velocity for ith particle

$$\begin{aligned} \boldsymbol{v}_i(t + \Delta t) &= \boldsymbol{v}_i(t) + \frac{1}{m_i} \int_t^{t+\Delta t} \boldsymbol{\Psi}_i^{tot} \, dt \\ &\approx \boldsymbol{v}_i(t) + \frac{\Delta t}{m_i} \left(\phi \, \boldsymbol{\Psi}_i^{tot}(t + \Delta t) + (1 - \phi) \, \boldsymbol{\Psi}_i^{tot}(t) \right), \end{aligned} \tag{4.1}$$

and the position for the by applying the integration process again:

$$\boldsymbol{r}_i(t + \Delta t) \approx \boldsymbol{r}_i(t) + \Delta t (\phi \boldsymbol{v}_i(t + \Delta t) + (1 - \phi) \boldsymbol{v}_i(t)), \tag{4.2}$$

which can be written as

$$\boldsymbol{r}_i(t + \Delta t) = \boldsymbol{r}_i(t) + \boldsymbol{v}_i(t) \Delta t + \frac{\phi (\Delta t)^2}{m_i} \left(\phi \, \boldsymbol{\Psi}_i^{tot}(t + \Delta t) + (1 - \phi) \, \boldsymbol{\Psi}_i^{tot}(t) \right), \tag{4.3}$$

which leads to a coupled set equations for $i = 1, 2, 3, \ldots, N_p$ particles. This system will be solved iteratively, furthering approaches found in Zohdi [16–52]. Accordingly, we write Eq. (4.3) in a more algorithmic form

$$\boldsymbol{r}_i^{L+1} = \boldsymbol{r}_i^{L} + \boldsymbol{v}_i^{L}\Delta t + \frac{\phi(\Delta t)^2}{m_i}\left(\phi(\boldsymbol{\Psi}_i^{tot,L+1}) + (1-\phi)(\boldsymbol{\Psi}_i^{tot,L})\right), \tag{4.4}$$

where the superscript L is a time-step counter. Because the particle mixture configuration system can significantly change during the deposition process, time-step adaptation is crucial. Within a time-step, the solution steps are, based on a global fixed-point iteration (Appendix C provides details on this solution process.):

- (1): Set $i = 1$ (particle counter) and $K = 0$ (iteration counter):
- (2): If $i > N_p$ then go to (4)
- (3): If $i \leq N_p$ then (a) compute position $\boldsymbol{r}_i^{L+1,K}$ and (b) go to (2) for next particle ($i = i + 1$)
- (4): Compute iterative error metrics (see Appendix C):

$$Z_K \stackrel{\text{def}}{=} \frac{\varpi_K}{TOL_r} \text{ and } \Lambda_K \stackrel{\text{def}}{=} \left(\frac{(\frac{TOL}{\varpi_0})^{\frac{1}{pK_d}}}{(\frac{\varpi_K}{\varpi_0})^{\frac{1}{pK}}}\right), \tag{4.5}$$

  where $\varpi_K \stackrel{\text{def}}{=} \frac{\sum_{i=1}^{N_p}\|\boldsymbol{r}_i^{L+1,K} - \boldsymbol{r}_i^{L+1,K-1}\|}{\sum_{j=1}^{N_p}\|\boldsymbol{r}_i^{L+1,K} - \boldsymbol{r}_i^{L}\|}$.
- (5): If $Z_K \leq 1$ (met tolerance) and $K < K_d$ (below preset number of iterations): (a) increment time: $t = t + \Delta t$, (b) construct the next time step: $(\Delta t)^{new} = \Lambda_K(\Delta t)^{old}$, (c) select the minimum size: $\Delta t = \textbf{MIN}((\Delta t)^{lim}, (\Delta t)^{new})$ and (d) update the particle positions and go to (1)
- (6): If $Z_K > 1$ (tolerance not met) and $K < K_d$ (still iterating) then (a) update the iteration counter: $K = K+1$, (b) reset the particle counter: $i = 1$ and (c) go to (2)
- (7): If $Z_K > 1$ (tolerance not met) and $K = K_d$ (at the iteration counter limit) then (a) construct a new time step: $(\Delta t)^{new} = \Lambda_K(\Delta t)^{old}$ and (b) restart at time t and go to (1).

We observe that in step (5), Λ_K may enlarge the time-step if the error is lower than the preset tolerance. Thus, because the scheme can also enlarge the time-steps if the iterative system converges quickly within an existing time step, to ensure the accuracy of the time-stepping scheme, we add an upper bound to control temporal discretization error, i.e., $\Delta t \leq \Delta t^{lim}$.

5. Thermal fields

5.1. Heat-transfer model

We assume that (infrared) radiative, convective and strain-rate effects are negligible for the particle's thermodynamics. Only laser-input heating and conduction are considered important. Thus, for each particle $i = 1, 2, \ldots, N_p$,

$$m_i C_i \dot{\theta}_i = \mathcal{Q}_i + \mathcal{H}_i, \tag{5.1}$$

where $\mathcal{Q}_i$ represents the conductive contribution from surrounding particles in contact (including walls), and $\mathcal{H}_i$ represents the external heating term. It is assumed that the temperature fields are uniform within the (small) particles. This assumption is justified, i.e. a lumped thermal model, ignoring temperature gradients and assuming a uniform temperature within a particle, when the Biot number is small. The Biot number for spheres scales with the ratio of the particle volume (V) to the particle surface area (A_s), $\frac{V}{A_s} = \frac{\frac{4}{3}\pi R^3}{4\pi R^2} = \frac{R}{3}$, which indicates that a uniform temperature distribution is appropriate, since the particles, by definition, are small. Assuming that the fields are uniform in each particle allows for the following (for particle i)

$$\mathcal{Q} = -\int_{\partial\omega} \boldsymbol{Q}\cdot\boldsymbol{n}\, dA \approx \sum_{j=1}^{N_{pc}} \mathbb{K}_{ij}\frac{\theta_j - \theta_i}{\|\boldsymbol{r}_i - \boldsymbol{r}_j\|}A_{ij}^c, \tag{5.2}$$

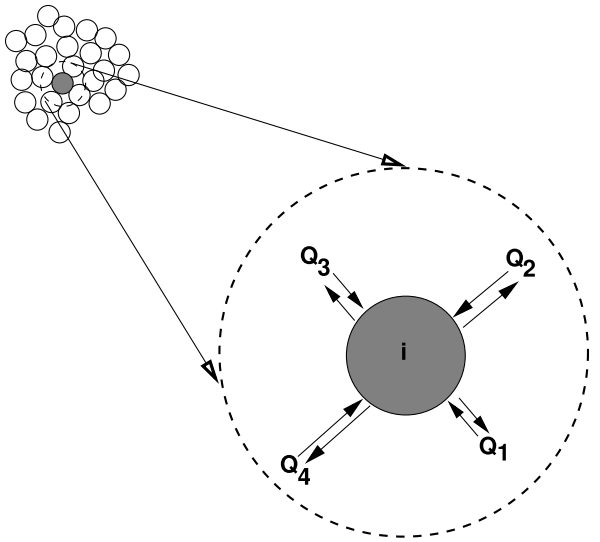

Fig. 5. Heat flux exchange for a particle induced by neighboring particles in contact.

where the summation extends over all particles $j = 1, 2, 3, \ldots, N_{pc}$ that are in contact with particle i (Fig. 5).[7] This yields

$$m_i C_i \frac{d\theta_i}{dt} = \underbrace{\sum_{j=1}^{N_{pc}} \mathbb{K}_{ij} \frac{\theta_j - \theta_i}{\|\boldsymbol{r}_i - \boldsymbol{r}_j\|} A_{ij}^c}_{\mathcal{Q}_i} + \mathcal{H}_i, \tag{5.3}$$

where the specific form of laser-induced heating is

$$\mathcal{H}_i \approx a_i I_i V_i, \tag{5.4}$$

where $a I_i$ is the absorbed laser-input for particle i and $0 \leq a_i \leq 1$ is an absorption constant. More remarks on laser-input will be given next.

5.2. Laser penetration and heating

As before in the beginning of this paper, we opt for a utilization of the Beer–Lambert law (see Eqs. (2.6), (2.7) and Fig. 2). One can modify Eq. (2.7) to account for a particle at depth ζ from particle interference from above the particle in question by determining the intersections with particles above particle at depth ζ, for example, $\zeta^* = \sum_{i=1}^{N} \Delta\zeta_i$ and modifying the Beer–Lambert relation to read

$$I(\zeta) = I_o e^{-a\zeta^*}. \tag{5.5}$$

It is possible to utilize discretization of the irradiant beam into rays and performing a full-blown ray-tracking scheme (see Zohdi [79,80,82]) or discretization of the beam into its electromagnetic field components via Maxwell's equations (see Zohdi [16,78]), However, these two approaches provide extremely detailed field information at the smallest scales. They are extraordinarily computationally expensive, and for the applications in this work, unwarranted. This leaves the Beer–Lambert framework, which we will employ for the remainder of the work. In such an approach, one can easily introduce nonuniform beam profiles, for example

$$I(d) = I(d = 0) e^{-bd}, \tag{5.6}$$

[7] $\mathbb{K}_{ij}$ can be approximated by an average interfacial value of the $i - j$ pair, $\mathbb{K}_{ij} \approx \frac{\mathbb{K}_i + \mathbb{K}_j}{2}$. If the materials are the same, this collapses to simply $\mathbb{K}$. As for the mechanical contact, A_{ij}^c is the contact area associated with the particle pair (ij).

where d is the distance from the center of the incident beam line. In the case of $b = 0$ we recapture a flat beam, $I(d) = I(d = 0)$.

5.3. Numerical integration

Integrating the energy equation yields, for each particle ($i = 1, 2, \ldots, N_p$) yields

$$\theta_i(t + \Delta t) = \theta_i(t) + \frac{1}{m_i C_i}\left(\int_t^{t+\Delta t} \mathcal{Q}_i \, dt + \int_t^{t+\Delta t} \mathcal{H}_i \, dt\right)$$
$$\approx \theta_i(t) + \frac{\Delta t}{m_i C_i}\left(\phi(\mathcal{Q}_i(t + \Delta t) + \mathcal{H}_i(t + \Delta t)) + (1 - \phi)(\mathcal{Q}_i(t) + \mathcal{H}_i(t))\right). \tag{5.7}$$

We note that Eq. (5.7) represents a coupled system of the general form (similar to the equation that arises for the particle dynamics)

$$\theta_i(t + \Delta t) = \mathcal{G}_i(\theta_i(t + \Delta t)) + \mathcal{R}_i, \tag{5.8}$$

where for the "remainder" term, $\mathcal{R}_i \neq \mathcal{R}_i(\theta_i(t + \Delta t))$, and where $\mathcal{G}_i$'s behavior is controlled by the magnitude of Δt. Clearly, the temperature is coupled to the mechanical behavior of the system. Shortly, we develop a multiphysical staggering scheme to solve the overall system.

6. Total system coupling: multiphysical staggering scheme

We now extend the iterative solution process introduced earlier for the particle dynamics to a multifield setting by (at a given time increment): (1) solving each field equation individually, "freezing" the other (coupled) fields in the system, allowing only the primary field to be active and (2) updating the primary field variable after the solution of each field equation. The next field equation is treated in a similar manner where, as the physics changes, the field that is most sensitive (exhibits the largest amount of relative nondimensional change) dictates the time-step size. This is an implicit, staggered, adaptive time-stepping scheme. Such approaches have a long history in the computational mechanics community. For example, Zienkiewicz [17], Zienkiewicz et al. [18], Lewis et al. [19], Lewis and Schrefler [20], Park and Felippa [21], Farhat et al. [22], Farhat and Lesoinne [23], Farhat et al. [24], Piperno [25], Piperno et al. [26], Piperno and Farhat [27] and Michopoulos et al. [28], Lesoinne and Farhat [29] and Le Tallec and Muoro [30].

6.1. A general iterative framework

The staggering scheme introduced earlier utilizes approaches found in Zohdi [16–52] and proceeds by considering an abstract setting, whereby one solves for the particle positions, assuming the thermal fields fixed,

$$\mathcal{A}_1(\underline{\boldsymbol{r}^{L+1,K}}, \theta^{L+1,K-1}) = \mathcal{F}_1(\boldsymbol{r}^{L+1,K-1}, \theta^{L+1,K-1}), \tag{6.1}$$

then one solves for the thermal fields, assuming the particle positions fixed,

$$\mathcal{A}_2(\boldsymbol{r}^{L+1,K}, \underline{\theta^{L+1,K}}) = \mathcal{F}_2(\boldsymbol{r}^{L+1,K}, \theta^{L+1,K-1}), \tag{6.2}$$

where only the underlined variable is "active", L indicates the time step and K indicates the iteration counter. Within the staggering scheme, implicit time-stepping methods, with time step size adaptivity, will be used throughout the upcoming analysis. We define the normalized errors within each time step, for the two fields,

$$\varpi_{rK} \stackrel{\text{def}}{=} \frac{\|\boldsymbol{r}^{L+1,K} - \boldsymbol{r}^{L+1,K-1}\|}{\|\boldsymbol{r}^{L+1,K} - \boldsymbol{r}^{L}\|} \quad \text{and} \quad \varpi_{\theta K} \stackrel{\text{def}}{=} \frac{\|\theta^{L+1,K} - \theta^{L+1,K-1}\|}{\|\theta^{L+1,K} - \theta^{L}\|}. \tag{6.3}$$

We define maximum "violation ratio", i.e. as the larger of the ratios of each field variable's error to its corresponding tolerance, by $Z_K \stackrel{\text{def}}{=} \mathbf{MAX}(z_{rK}, z_{\theta K})$, where

$$z_{rK} \stackrel{\text{def}}{=} \frac{\varpi_{rK}}{TOL_r} \quad \text{and} \quad z_{\theta K} \stackrel{\text{def}}{=} \frac{\varpi_{\theta K}}{TOL_\theta}, \tag{6.4}$$

with the minimum scaling factor defined as $\Lambda_K \stackrel{\text{def}}{=} \textbf{MIN}(\Lambda_{rK}, \Lambda_{\theta K})$, where

$$\Lambda_{rK} \stackrel{\text{def}}{=} \left(\frac{(\frac{TOL_r}{\varpi_{r0}})^{\frac{1}{pK_d}}}{(\frac{\varpi_{rK}}{\varpi_{r0}})^{\frac{1}{pK}}} \right), \qquad \Lambda_{\theta K} \stackrel{\text{def}}{=} \left(\frac{(\frac{TOL_\theta}{\varpi_{\theta 0}})^{\frac{1}{pK_d}}}{(\frac{\varpi_{\theta K}}{\varpi_{\theta 0}})^{\frac{1}{pK}}} \right). \tag{6.5}$$

6.2. Overall solution algorithm

The algorithm is as follows:

(1) GLOBAL FIXED − POINT ITERATION : (SET i = 1 AND K = 0) :
(2) IF i > N_p THEN GO TO (4)
(3) IF i ≤ N_p THEN : (FOR PARTICLE i)
(a) COMPUTE POSITION :$\boldsymbol{r}_i^{L+1,K}$
(b) COMPUTE TEMPERATURE :$\theta_i^{L+1,K}$
(c) GO TO (2) AND NEXT PARTICLE (i = i + 1)
(4) ERROR MEASURES(normalized) :
(a)$\varpi_{rK} \stackrel{\text{def}}{=} \frac{\sum_{i=1}^{N_p} \|\boldsymbol{r}_i^{L+1,K} - \boldsymbol{r}_i^{L+1,K-1}\|}{\sum_{i=1}^{N_p} \|\boldsymbol{r}_i^{L+1,K} - \boldsymbol{r}_i^{L}\|}$
$\varpi_{\theta K} \stackrel{\text{def}}{=} \frac{\sum_{i=1}^{N_p} \|\theta_i^{L+1,K} - \theta_i^{L+1,K-1}\|}{\sum_{i=1}^{N_p} \|\theta_i^{L+1,K} - \theta_i^{L}\|}$
(b)$Z_K \stackrel{\text{def}}{=} \textbf{MAX}(z_{rK}, z_{\theta K})$ $where$ $z_{rK} \stackrel{\text{def}}{=} \frac{\varpi_{rK}}{TOL_r}$, $z_{\theta K} \stackrel{\text{def}}{=} \frac{\varpi_{\theta K}}{TOL_\theta}$
(c)$\Lambda_K \stackrel{\text{def}}{=} \textbf{MIN}(\Lambda_{rK}, \Lambda_{\theta K})$ $where$
$\Lambda_{rK} \stackrel{\text{def}}{=} \left(\frac{(\frac{TOL_r}{\varpi_{r0}})^{\frac{1}{pK_d}}}{(\frac{\varpi_{rK}}{\varpi_{r0}})^{\frac{1}{pK}}} \right)$,
$\Lambda_{\theta K} \stackrel{\text{def}}{=} \left(\frac{(\frac{TOL_\theta}{\varpi_{\theta 0}})^{\frac{1}{pK_d}}}{(\frac{\varpi_{\theta K}}{\varpi_{\theta 0}})^{\frac{1}{pK}}} \right)$ (6.6)
(5)IF TOL. NOT MET ($Z_K > 1$) AND $K < K_d$ REPEAT ITERATION (K = K + 1)
(6) IF TOL. MET ($Z_K \leq 1$) AND $K < K_d$ THEN :
(a) INCREMENT TIME : $t = t + \Delta t$
(b) CONSTRUCT NEW TIME STEP : $\Delta t = \Lambda_K \Delta t$,
(c) SELECT MINIMUM : $\Delta t = \textbf{MIN}(\Delta t^{lim}, \Delta t)$
(d) UPDATE LASER FIELD I_i (FOR ALL PARTICLES ITERATIVELY)
(e) AND GO TO (1)
(7) IF TOL. NOT MET ($Z_K > 1$) AND $K = K_d$ THEN :
(a) CONSTRUCT NEW TIME STEP :$\Delta t = \Lambda_K \Delta t$
(b) UPDATE LASER FIELD I_i (FOR ALL PARTICLES ITERATIVELY)
(c) RESTART AT TIME = t AND GO TO (1)

The overall goal is to deliver solutions where staggering (incomplete coupling) error is controlled and the temporal discretization accuracy dictates the upper limits on the time step size (Δt^{lim}).

Remark. The use of so-called interaction lists is advantageous to speed-up calculations and to extend such simulations to very large particle systems. These lists are constructed, for each particle, by taking neighboring particles within a radius of influence. The list is then updated periodically during the simulations. This significantly reduces the computation time used in contact search and other intra-particle calculations, which are N^2 operations. In the simulations that were presented: (a) For each particle, a nearest-neighbor list was constructed at the beginning of the simulation (b) For a subinterval of time, the interaction for each particle was restricted to these neighbors and (c) the lists were updated after that interval expired and the process repeated. See Zohdi [82–88] for details. (See Fig. 6.)

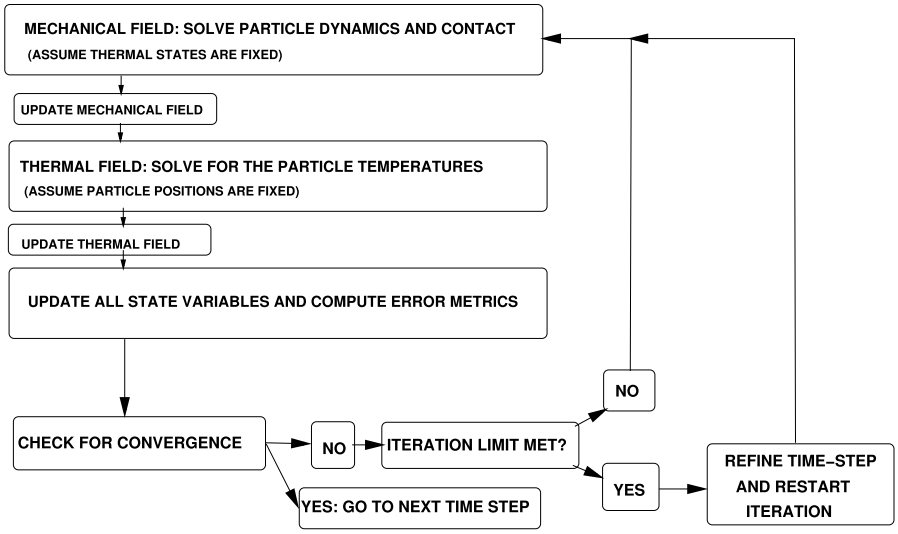

Fig. 6. A flow chart for the modular, staggered, computation.

7. Numerical examples of involving polydisperse depositions

In order to characterize the physical process, we select a model problem, where we consider a group of N_p spherical particles, of two sizes, randomly dispersed, and initially generated within in a cylindrical domain of normalized radius $R = 1$ (diameter $D = 2R = 2$) and length $L = 8$ (Fig. 7). The ratio of smaller particle diameter, d_s, to total domain diameter, D, was $d_s/D = 0.05$ for and $d_l/D = 0.2$ for the larger particles. A Random Sequential Addition (RSA) algorithm (Widom [31]) was employed to initially to place particles in the domain. Thereafter, the dynamics of the particles drove them to a more compacted state.[8] Although we have formulated the system with a both a simultaneous electromagnetic field, for the examples of interest, consistent with most mainstream industrial processes, we will only include the electric field in the simulations. There are of course applications where an applied magnetic field would be of interest, however, this is beyond the scope of the current paper. Table 1 shows the simulation parameters that were chosen.[9]

For example, the normal stiffness constant for the ith and jth particles in the contact law can be written as (here Θ is the temperature, which is fixed in the present analysis and Θ^* is a thermal constant):

$$K_{pi} = \mathbf{MAX}(K_{pio}\left(e^{-a_i(\frac{\Theta_i}{\Theta_i^*}-1)}\right), K_{pi}^{lim}), \tag{7.1}$$

and for particle j

$$K_{pj} = \mathbf{MAX}(K_{pjo}\left(e^{-a_j(\frac{\Theta_j}{\Theta_j^*}-1)}\right), K_{pj}^{lim}), \tag{7.2}$$

and the average taken at the interface, providing the parameter needed in the contact law, $K_{pij} = \frac{1}{2}\left(K_{pi} + K_{pj}\right)$. In the current example, $K_{po} = 10^7$ N/m^2, where $K_p = \mathbf{MAX}(K_{po}\left(e^{-(a\frac{\Theta}{\Theta^*}-1)}\right), K_p^{lim})$, where $\Theta^* = 500$ °K, $K_p^{lim} = 10^6$ N/m^2, exponent in the contact law was set to $p_p = 2$ (the temperature was fixed to be $\Theta = 300$ °K and the thermal sensitivity parameter was set to $a = 1$). There are many possible representations for temperature-dependency. The overall model has a modular structure which allows one to replace models easily. We refer the reader to Zohdi [79–82] for more details in the general area of thermal multiphysics.

[8] For more details on packing of particles, see Torquato [32], Kansaal et al. [33] and Donev et al. [102–106].

[9] This parameter set is not intended to simulate any specific scenario. The units are SI — with properties being the same for the small and large particles, unless explicitly stated otherwise. We note that no magnetic field was used in this example, $\boldsymbol{B}^{ext} = (0, 0, 0)$ Tesla.

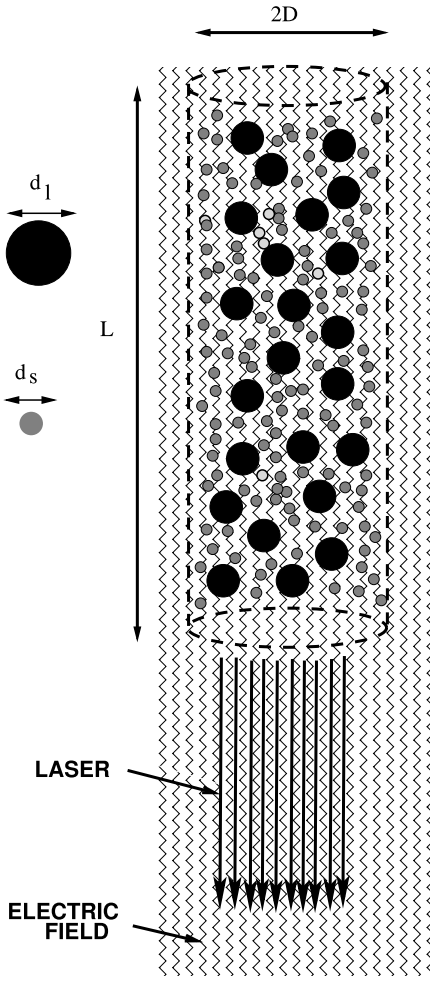

Fig. 7. Schematic of the initial configuration for the model problem.

Just to test illustrate the model problem, we allowed the laser to "raster" back and forth in the vertical $(x–y)$ plane, thus producing oscillatory heating (Figs. 7–12). An irradiance decay from the center of the lase was set to $b = 1$ in Eq. (5.6), thus it peaks in the center. For all the particles, we applied an initial velocity of $\boldsymbol{v}(t = 0) = (-1, 0, 0)$, projecting them directly towards the substrate, in conjunction with gravity ($\boldsymbol{g} = -(9.81, 0, 0)$ m/s^2). The electric field starts below a $y–z$ parallel flat plane at $(2, 0, 0)$. The center of the starting configuration is at $(3.5, 0, 0)$ and the substrate is at $(-2, 0, 0)$. In the upcoming simulations, the smaller particles are "binder" particles and the larger particles are "functionalizing" particles. We considered an external electric field and particle-to-particle ionization interaction effects. In this case the particle system falls due to initial starting velocity and the electric field. The mutual ionization forces the stream collapse upon itself and break into two distinct "droplets", which then reconnect to form a single large droplet that continues to fall to attach to the substrate. The impact with the substrate is controlled by the electric field, which pins the material to the substrate (Figs. 8–12). There is a direct correlation with the ionization strength between particles in the powder and the more fluid-like behavior, which the electric field can control. It is important to note that in the analysis of standard (nonparticulate) fluids, the breakup of a long column of fluid with perturbations (longitudinal waviness) was first investigated experimentally by Plateau in 1873, who found that a vertically falling stream of water will break up into drops if its wavelength is greater than approximately 3.13–3.18 times its diameter. Thereafter, Rayleigh analytically proved that a wavy falling column of non-viscous liquid (with circular cross-section) should break up into drops if its wavelength exceeded its circumference. This

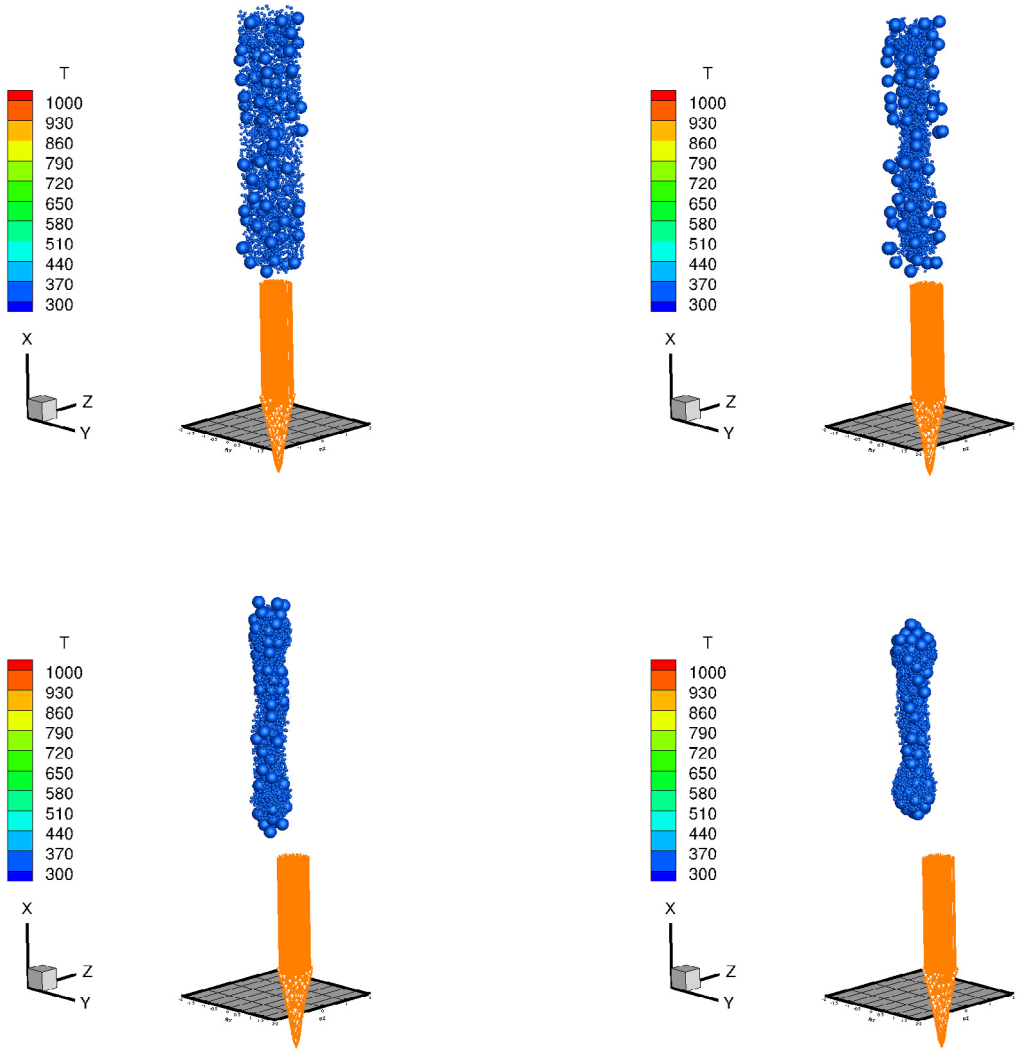

Fig. 8. External electric field and particle-to-particle ionization interaction. The laser is moving back and forth in the $x-y$ plane.

"unstable" phenomena is driven by surface tension, which forces fluids to minimize their surface area. We refer the reader to Papageorgiou [34] and Eggers [35] for more details. In the case of a charged particulate medium, the degree of near-field strength plays the role of surface tension. Clearly, an uncharged particulate medium will not exhibit this phenomenon. In Zohdi [36], several other deposition scenarios were considered (without lasers or thermal effects), such as (1) dynamics with no external electric field and no particle-to-particle ionization interaction effects, (2) dynamics with an external electric field and no particle-to-particle ionization interaction effects and (3) dynamics with no external electric field and particle-to-particle ionization interaction effects, etc. With no ionization, the system behaves as a loose powder, which is nearly impossible to control as a deposition. As the ionization is increased, the balance between mutual attraction and repulsion leads to surface tension like effects yielding coherent aggregate "droplets" of the powder-mixture material. In terms of computational performance, the simulation utilized 10 030 time steps and 35 633 fixed point interaction; roughly 3.5 fixed point iterations per time step. As we have mentioned previously, because the scheme can also enlarge the time-steps if the iterative system is converges quickly within an existing time step, to ensure the accuracy of the time-stepping scheme, we add an upper bound to control temporal discretization error, i.e., $\Delta t \leq \Delta t^{lim}$. We started all simulations with extremely small time step sizes, and allowed the error estimation and time-step adaptation to auto-correct to the proper size. Fig. 13 shows a typical scenario, taken

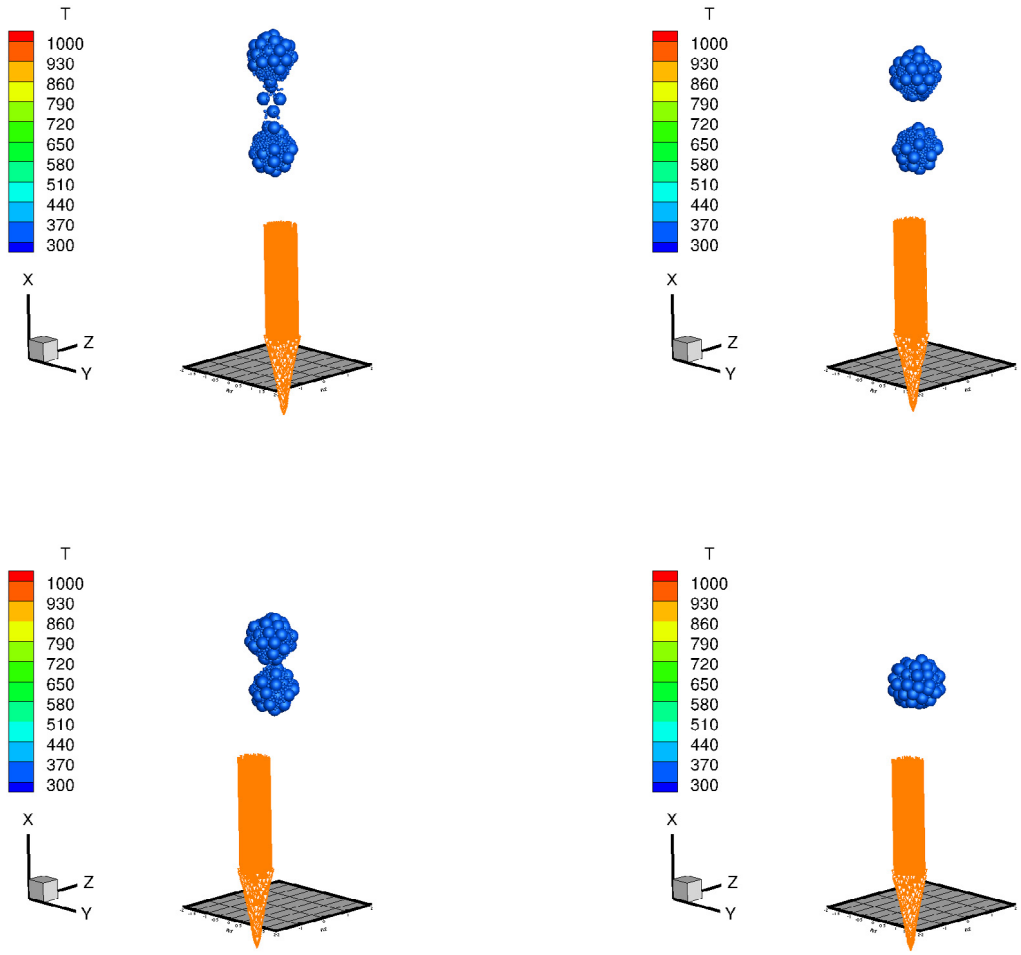

Fig. 9. External electric field and particle-to-particle ionization interaction. The laser is moving back and forth in the $x-y$ plane.

from the example. The step sizes were initially small and adapted according to the error estimate until they met the limit set by the algorithm (user specified). The time-steps were purposely started extremely small, since knowledge of the appropriate size is known a priori.

8. Summary and extensions

In summary, there are large numbers of applications in additive manufacturing that involve the dynamic deposition of powders and the in-flight heating of such material by a laser. The present work developed a modular discrete-element type multiphysics method for the simulation of the particle dynamics, interaction with a laser and detailed thermal behavior. The overall objective was to provide researchers with a framework to construct computational tools for this growing industry. In the approach pursued here, the overall particle-mixture system was constructed by coupling submodels for each primary physical process together and an iterative staggering scheme was developed whereby, within every time step, each individual particle was solved, "freezing" the state of the remaining multiparticle system. Thereafter, the state of the particle was then updated and the algorithm moved to the next particle in the system and the process was repeated. The overall process moved through the entire system repeatedly until convergence in an appropriate norm. As the system evolved, an error estimate dictates the time-step size that is needed to induce convergence to below an appropriate error level. The construction of model and solution process was modular, thus one can easily replace physical submodels with other choices, making it easy to numerically experiment with a variety of models. Extensions to this type of analysis could include parameter studies on the changes in dynamics due to

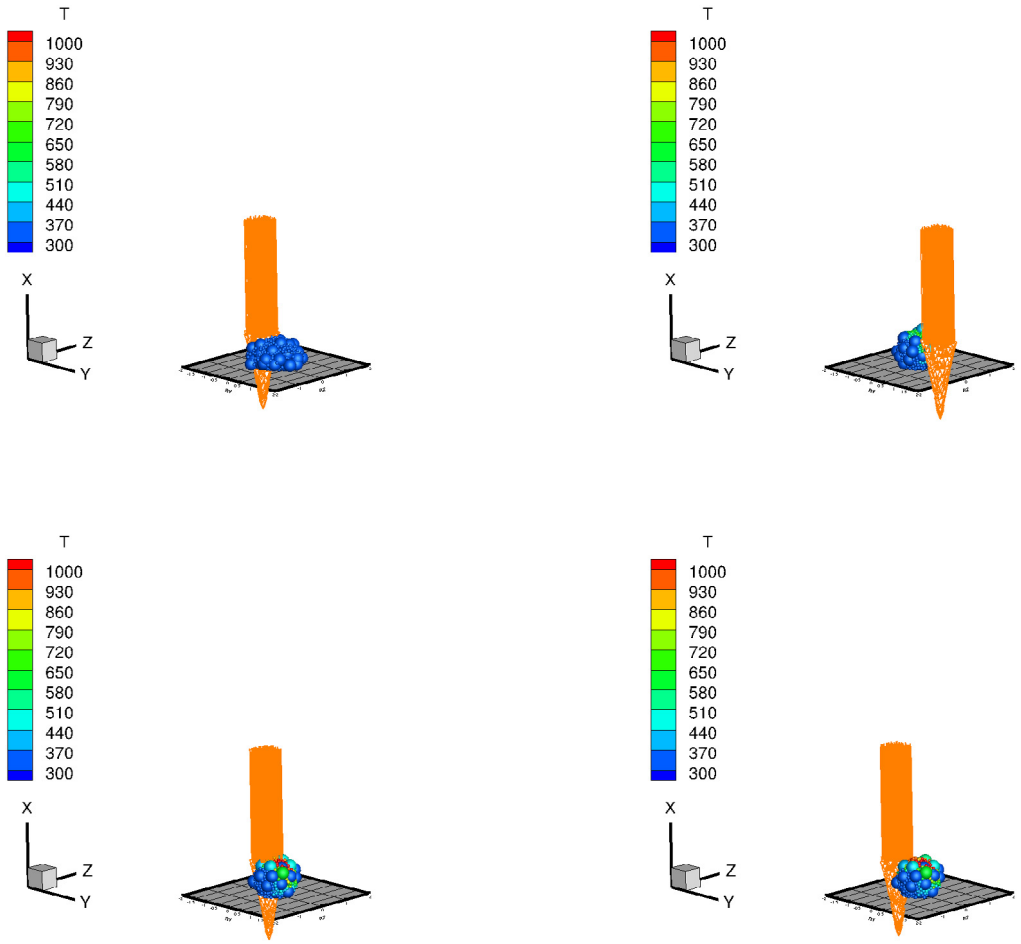

Fig. 10. External electric field and particle-to-particle ionization interaction. The laser is moving back and forth in the $x-y$ plane.

strong magnetic fields. Although magnetic fields are somewhat less used than electric fields for deposition, they have certain unique utility by being able to "bend" sprays and depositions (see Martin [53,54] for the state of the art). Other advanced manufacturing processes of interest can involve particle-mixtures that may be highly saturated with an interstitial fluid or embedded within a fluid medium, thus necessitating a particle–fluid interaction framework. This will require a spatio-temporal discretization by employing Finite Element, Finite Difference or Finite Volume methods coupled to Discrete Elements. We refer the reader to Oñate et al. [5–7], Avci and Wriggers [37], Leonardi et al. [38], Oñate et al. [7], Bolintineanu et al. [39] and Zohdi [87,90]. As mentioned earlier in the paper, the presented work focuses on the first of two overall "macrostages" of a complex manufacturing process using DEM. Specifically, dry-powder materials, which are of a discrete particulate character, were modeled using DEM for the deposition phase of the analysis. Other papers of the author (Zohdi [78–83]) have addressed stage two, namely phase transformations, curing (cooling) and stress analysis, using more appropriate continuum and hybrid DEM-continuum approaches.

A crucial extension/augmentation of the presented analysis is to ascertain the effective properties of the particle-functionalized materials after deposition, such as (1) the effective electrical conductivity, (2) the effective electrical permittivity and (3) the effective magnetic permeability. This is a rich subject and we refer the interested reader to Torquato [32], Jikov et al. [40], Hashin [41], Mura [42], Markov [43] for theoretical aspects and for more computationally-oriented approaches, Ghosh [44], Ghosh and Dimiduk [45], Zohdi and Wriggers [83], Zohdi [16] and recently, Matous et al. [46] for a review of the state-of-the-art in multiscale methods for nonlinear heterogeneous materials. The determination of effective properties of additive depositions is currently being pursued by the author. Finally, in closing, we remark that the employment of computational discrete and continuum micromechanical models

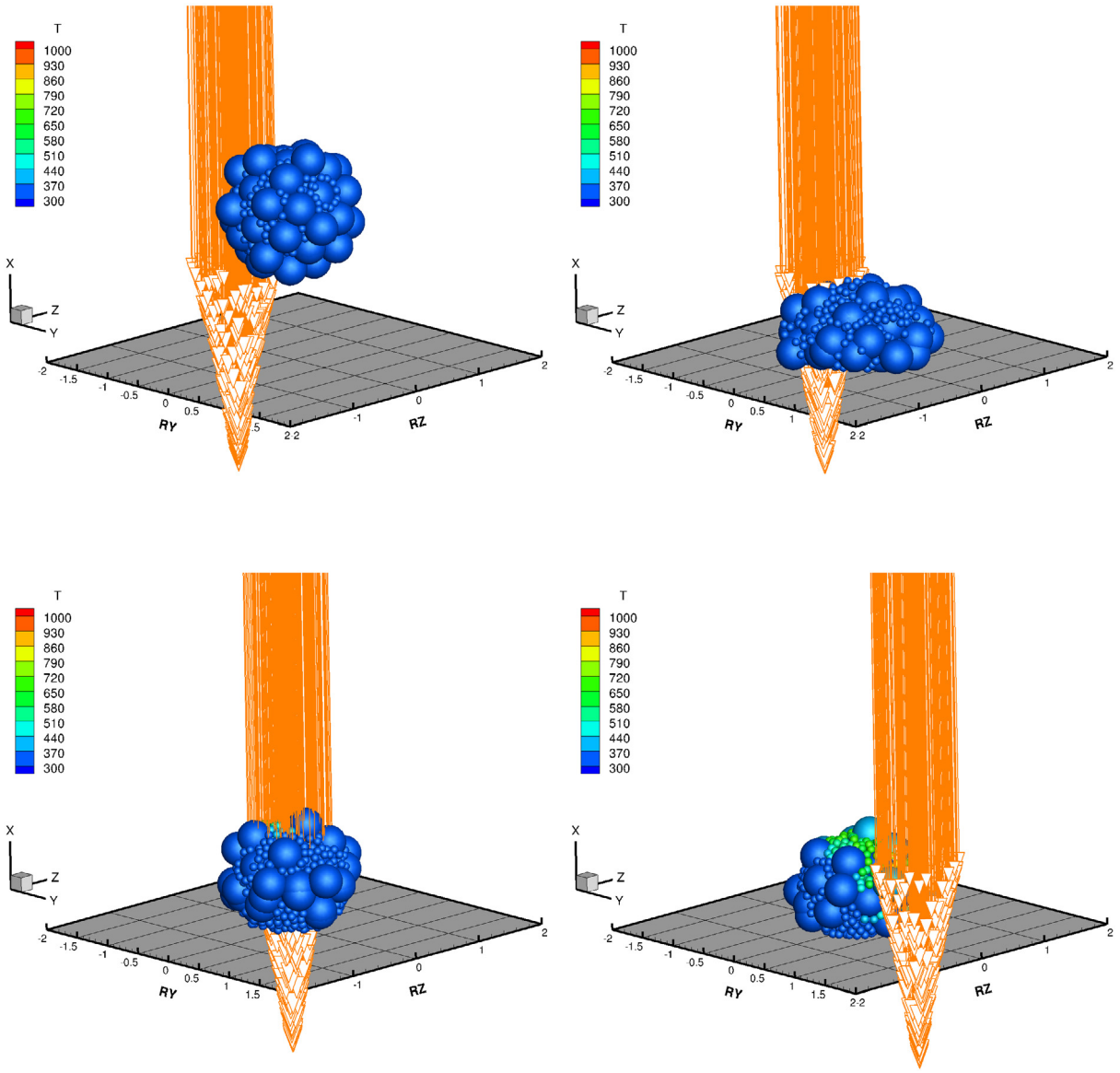

Fig. 11. ZOOM: External electric field and particle-to-particle ionization interaction. The laser is moving back and forth in the $x-y$ plane.

in multistage additive manufacturing and 3D printing can ultimately bring level of systemization and rigor that is now needed in this evolving field. In particular, because additive manufacturing and 3D printing are based on adding material, alone they are inadequate for high-precision applications and typically need be combined with classical subtractive manufacturing processes, as outlined in a recent US National Academies Report (Zohdi and Dornfeld [47]), thus necessitating highly coordinated multistage computational approaches.

Acknowledgments

This work was funded in part by the Army Research Laboratory through the Army High Performance Computing Research Center under cooperative agreement W911NF-07-2-0027, program manager Dr. Raju Namburu, and the Siemens corporation, through grant 85702-23845-44-EKZOH-EEZT85702X, under program manager Dr. Marco Brunelli.

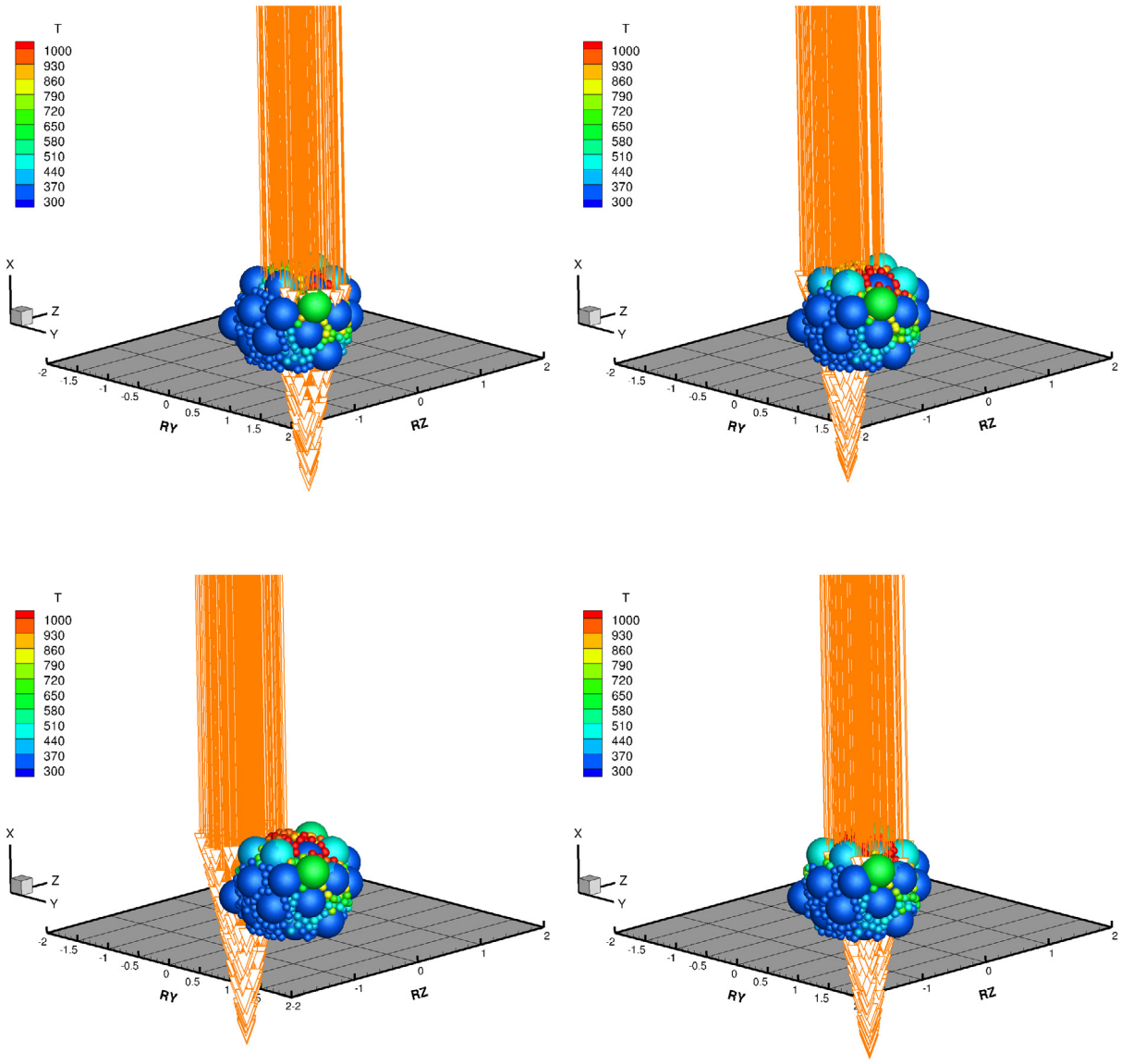

Fig. 12. ZOOM: External electric field and particle-to-particle ionization interaction. The laser is moving back and forth in the x–y plane.

Appendix A. Contact area parameter and alternative models

Following Zohdi [80,85–90], and referring to Fig. 4, one can solve for an approximation of the common contact radius a_{ij} (and the contact area, $A^c_{ij} = \pi a^2_{ij}$) by solving the following three equations: (a) $a^2_{ij} + L^2_i = R^2_i$, (b) $a^2_{ij} + L^2_j = R^2_j$ and (c) $L_i + L_j = \|\boldsymbol{r}_i - \boldsymbol{r}_j\|$, where R_i is the radius of particle i, R_j is the radius of particle j, L_i is the distance from the center of particle i and the common contact interpenetration line and L_j is the distance from the center of particle j and the common contact interpenetration line, where the extent of interpenetration is $\delta_{ij} = R_i + R_j - \|\boldsymbol{r}_i - \boldsymbol{r}_j\|$. The above equations yield an expression a_{ij}, which yields an expression for the contact area parameter

$$A^c_{ij} = \pi a^2_{ij} = \pi(R^2_i - L^2_i), \tag{A.1}$$

Table 1
Parameters used in the model problem.

Quantity	Value
Electric field	$\boldsymbol{E}^{ext} = (-100, 0, 0)$ N/C
Charge per unit particle surface area	$q = 100$ C/kg
Density of air	$\rho_g = 1.225$ kg/m^3
Particles, randomly distributed in parallelepiped domain	$(8 \times 2 \times 2)$ m
Total number of particles	$N = 2000$: 1900 small particles and 100 large particles
Radius of small particles	$R_s = 0.05$ m
Radius of large particles	$R_l = 0.2$ m
Density of materials	$\rho_1 = 2000$ kg/m^3 (binder particles), $\rho_2 = 5000$ kg/m^3 (functionalizing particles)
Contact damping parameter	$c^{cd} = 10^5$
Friction contact parameter	$K^f = 10^7$
Coefficient of static friction	$\mu_s = 0.4$
Coefficient of dynamic friction	$\mu_d = 0.3$
Normal bond parameter	$K^{nb} = 10^6$ N/m^2 and exponent set to $p_b = 2$
Rotational/tangential bond parameter	$K^{rb} = 10^3$
Near-field parameters	$\bar{\alpha}_1 = 0.5$, $\beta_1 = 1$, $\bar{\alpha}_2 = 0.01$, $\beta_2 = 2$ (where $\bar{\alpha}$ is per unit mass)
Heating absorption coefficient	$a = 0.5$
Conductivity	$\mathbb{K} = 100$ W/m K
Initial material temperature	$\theta_i(t = 0) = 300$ °K
Wall temperature	$\theta_w(t = 0) = 500$ °K
Heat capacity	$C = 100$ J/kg K
Initial irradiance per volume	$I_o = 10^{10}$ W/m^3
Total simulation event duration	1.0 s
Desired number of fixed point iterations	$K_d = 10$
Trapezoidal-like time-stepping parameter	$\phi = 0.5$
Initial time step size	$\Delta t = 0.0000025$ s
Time step upper bound	$\Delta t^{l-m} = 0.00025$ s
Tolerance for the fixed-point iteration	10^{-6}

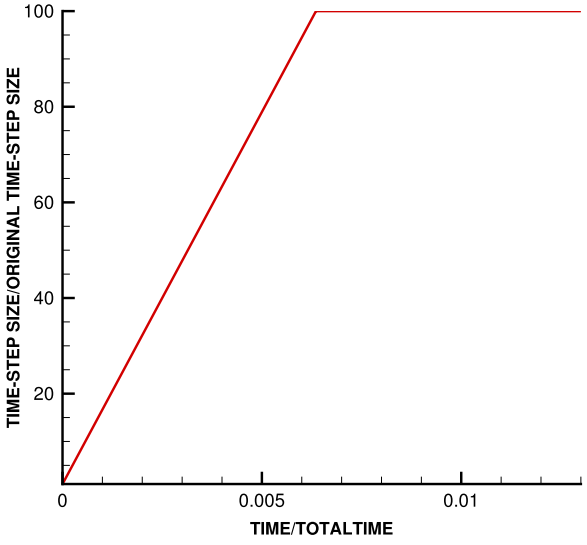

Fig. 13. Time-step adaptation for model problem. The step sizes were initially small and adapted according to the error estimate until they met the limit set by the algorithm (user specified). The time-steps were purposely started extremely small, since knowledge of the appropriate size is unknown a priori.

where $L_i = \frac{1}{2}\left(\|\boldsymbol{r}_i - \boldsymbol{r}_j\| - \frac{R_j^2 - R_i^2}{\|\boldsymbol{r}_i - \boldsymbol{r}_j\|}\right)$. Alternative models, building on Hertzian-contact which connect the relative proximity of the particles and other metrics to the contact force, $\boldsymbol{\Psi}_{ij}^{con,n} \propto \mathcal{F}(\boldsymbol{r}_i, \boldsymbol{r}_j, \boldsymbol{n}_{ij}, R_i, R_j, \ldots)$, building on, for

example, Hertzian contact models, can be implemented with no particular difficulty. For the remainder of the analysis, we shall use the deformation metric in Eq. (3.4). For detailed treatments, see Wellman et al. [108–112] and Avci and Wriggers [37]. We note that with the appropriate definition of parameters, one can recover Hertz, Bradley, Johnson–Kendel–Roberts, Derjaguin–Muller–Toporov contact models. For more details, we refer the reader to Johnson [48]. Clearly, a finer resolution of the deformation within a particle, it must be treated as a deformable continuum, requiring, for example the Finite Element Method for the contacting bodies. This requires a large computational effort that is beyond the scope of this paper (see Wriggers [49,50] and Zohdi and Wriggers [83]).

Appendix B. The effects of drag

For the drag that does not emanate from surrounding particles or that walls, we will employ a general phenomenological model

$$\boldsymbol{\Psi}_i^{drag} = \frac{1}{2}\rho_g C_D \|\boldsymbol{v}^g - \boldsymbol{v}_i\|(\boldsymbol{v}^g - \boldsymbol{v}_i)A, \tag{B.1}$$

where C_D is the drag coefficient, A is the reference area, which for a sphere is $A = \pi R^2$, ρ_g is the density of the ambient gas environment and $\boldsymbol{v}^g$ is the velocity of the surrounding medium which, in the case of interest, is air. Generally speaking, the drag coefficient, which is an empirical parameter which attempts to represent the action of the gas forces on an object, is not a constant, and would vary with, for example, the Reynolds number. In the zero Reynolds number limit the drag would be that of a Stokesian regime. One possible way to represent the drag coefficient is with a piecewise definition, as a function of the Reynolds number (Chow [51]):

- For $0 < Re \leq 1$, $C_D = \frac{24}{Re}$,
- For $1 < Re \leq 400$, $C_D = \frac{24}{Re^{0.646}}$,
- For $400 < Re \leq 3 \times 10^5$, $C_D = 0.5$,
- For $3 \times 10^5 < Re \leq 2 \times 10^6$, $C_D = 0.000366 Re^{0.4275}$,
- For $2 \times 10^6 < Re < \infty$, $C_D = 0.18$,

where the local Reynolds number for a particle is $Re \overset{\text{def}}{=} \frac{2R\rho_g \|\boldsymbol{v}^g - \boldsymbol{v}_i\|}{\mu_g}$ and μ_g is the gas viscosity. The viscosity coefficient for air is $\mu_g = 0.000018$ Pa/s. Using the hybrid model reduces the drag at the lower Reynolds number regimes, relative to simply picking a constant mid-range value for C_D (for example $C_D = 0.5$), thus producing less drag than a constant drag coefficient. The piecewise drag law of Chow [51] is a mathematical description for the Reynolds number over a wide range and is a curve-fit of extensive data from Schlichting [94]. As observed in the experimental data, the mathematical function exhibits a discontinuity at $Re = 3 \times 10^5$, although in an explosion the time a particle spends at this Reynolds number is almost negligible. In the low velocity (low Reynolds number) limit a Stokesian model is most appropriate, which is what the drag law above attempts to incorporate. The drag forces are significantly smaller with a Stokesian model. Comparing a purely Stokesian drag law, which would be valid for small particles and laminar flow (low Reynolds number)

$$\boldsymbol{\Psi}_i^{drag,Stokesian} = c(\boldsymbol{v}^g - \boldsymbol{v}_i) = \mu_g 6\pi R_i(\boldsymbol{v}^g - \boldsymbol{v}_i), \tag{B.2}$$

where μ_g is the gas viscosity. We observe the following:

$$\frac{\|\boldsymbol{\Psi}_i^{drag,Stokesian}\|}{\|\boldsymbol{\Psi}_i^{drag}\|} = \frac{12\mu_g}{\rho_g C_D R\|\boldsymbol{v}^g - \boldsymbol{v}_i\|}. \tag{B.3}$$

For typical parameters for air and spherical particles (using $C_D = 0.5$, which is a mid-range value from the piecewise drag law introduced earlier), we have

$$\frac{\|\boldsymbol{\Psi}_i^{drag,Stokesian}\|}{\|\boldsymbol{\Psi}_i^{drag}\|} = \frac{12\mu_g}{\rho_g C_D R\|\boldsymbol{v}^g - \boldsymbol{v}_i\|} \approx \frac{0.0004}{R\|\boldsymbol{v}^g - \boldsymbol{v}_i\|}, \tag{B.4}$$

which indicates that for extremely small particles and low velocities, the Stokesian model dominates, while for larger particles and large velocities, the phenomenological model dominates.

In order to determine the relative strengths of the gas drag force to the electromagnetic forces acting on the particle, consider the following model for an isolated particle:

$$m\dot{\boldsymbol{v}} = \boldsymbol{\Psi}^{drag} + \boldsymbol{\Psi}^{e+m} = C_D \frac{1}{2} A \rho_g \|\boldsymbol{v}^g - \boldsymbol{v}\|^2 \boldsymbol{\tau} + \bar{q}\rho_p V(\boldsymbol{E}^{ext} + \boldsymbol{v} \times \boldsymbol{B}^{ext}), \tag{B.5}$$

where $\bar{q}$ is the charge per unit mass, ρ_p is the density of the particle and $V = \frac{4}{3}\pi R^3$. The general ratio is

$$\lambda(\boldsymbol{v}) \stackrel{\text{def}}{=} \frac{\|\boldsymbol{\Psi}^{e+m}\|}{\|\boldsymbol{\Psi}^{drag}\|} = \frac{\|\bar{q}\rho_p V(\boldsymbol{E}^{ext} + \boldsymbol{v} \times \boldsymbol{B}^{ext})\|}{C_D \frac{1}{2} A \rho_g \|\boldsymbol{v}^g - \boldsymbol{v}\|^2} = \frac{8|\bar{q}|\rho_p R}{3 C_D \rho_g} \left(\frac{\|\boldsymbol{E}^{ext} + \boldsymbol{v} \times \boldsymbol{B}^{ext}\|}{\|\boldsymbol{v}^g - \boldsymbol{v}\|^2} \right). \tag{B.6}$$

Using the Triangle and Cauchy–Schwarz inequalities:

$$\lambda(\boldsymbol{v}) \leq \frac{8|\bar{q}|\rho_p R}{3 C_D \rho_g} \left(\frac{\|\boldsymbol{E}^{ext}\| + \|\boldsymbol{v}\|\|\boldsymbol{B}^{ext}\|}{\|\boldsymbol{v}^g - \boldsymbol{v}\|^2} \right), \tag{B.7}$$

which leads to

$$\|\boldsymbol{E}^{ext}\| + \|\boldsymbol{v}\|\|\boldsymbol{B}^{ext}\| \geq \lambda(\boldsymbol{v}) \frac{3 C_D \rho_g \|\boldsymbol{v}^g - \boldsymbol{v}\|^2}{8|\bar{q}|\rho_p R}. \tag{B.8}$$

If we set $\lambda = 1$, we obtain an expression for the electromagnetic forces to have parity with the drag force. In the case when the magnetic field is negligible, we have:

$$\|\boldsymbol{E}^{ext}\| = \frac{3 C_D \rho_g \|\boldsymbol{v}^g - \boldsymbol{v}\|^2}{8|\bar{q}|\rho_p R}. \tag{B.9}$$

In the case when the electric field is negligible, we have

$$\|\boldsymbol{B}^{ext}\| \geq \frac{3 C_D \rho_g \|\boldsymbol{v}^g - \boldsymbol{v}\|^2}{8|\bar{q}|\rho_p R \|\boldsymbol{v}\|}. \tag{B.10}$$

Appendix C. Iterative methods

The system represented by Eq. (4.4) can be iteratively solved by recasting it in the following form

$$\boldsymbol{r}_i^{L+1,K} = \boldsymbol{r}_i^L + \boldsymbol{v}_i^L \Delta t + \frac{(\phi \Delta t)^2}{m_i} \boldsymbol{\Psi}_i^{tot,L+1,K-1} + \frac{\phi(\Delta t)^2}{m_i}(1-\phi)\boldsymbol{\Psi}_i^{tot,L}, \tag{C.1}$$

which is of the form

$$\boldsymbol{r}_i^{L+1,K} = \mathcal{G}(\boldsymbol{r}_i^{L+1,K-1}) + \mathcal{L}_i, \tag{C.2}$$

where $K = 1, 2, 3, \ldots$ is the index of iteration within time step $L+1$ and

- $\boldsymbol{\Psi}_i^{tot,L+1,K-1} \stackrel{\text{def}}{=} \boldsymbol{\Psi}_i^{tot,L+1,K-1}(\boldsymbol{r}_1^{L+1,K-1}, \boldsymbol{r}_2^{L+1,K-1} \ldots \boldsymbol{r}_N^{L+1,K-1})$,
- $\boldsymbol{\Psi}_i^{tot,L} \stackrel{\text{def}}{=} \boldsymbol{\Psi}_i^{tot,L}(\boldsymbol{r}_1^L, \boldsymbol{r}_2^L \ldots \boldsymbol{r}_N^L)$,
- $\mathcal{G}(\boldsymbol{r}_i^{L+1,K-1}) = \frac{(\phi \Delta t)^2}{m_i} \boldsymbol{\Psi}_i^{tot,L+1,K-1}$ and
- $\mathcal{L}_i = \boldsymbol{r}_i^L + \boldsymbol{v}_i^L \Delta t + \frac{\phi(\Delta t)^2}{m_i}(1-\phi)\boldsymbol{\Psi}_i^{tot,L}$.

The term $\mathcal{L}_i$ is a remainder term that does not depend on the solution. The convergence of such a scheme is dependent on the behavior of $\mathcal{G}$. Namely, a sufficient condition for convergence is that $\mathcal{G}$ is a contraction mapping for all $\boldsymbol{r}_i^{L+1,K}$, $K = 1, 2, 3 \ldots$ In order to investigate this further, we define the iteration error as

$$\varpi_i^{L+1,K} \stackrel{\text{def}}{=} \boldsymbol{r}_i^{L+1,K} - \boldsymbol{r}_i^{L+1}. \tag{C.3}$$

A necessary restriction for convergence is iterative self-consistency, i.e. the "exact" (discretized) solution must be represented by the scheme, $\boldsymbol{r}_i^{L+1} = \mathcal{G}(\boldsymbol{r}_i^{L+1}) + \mathcal{L}_i$. Enforcing this restriction, a sufficient condition for convergence is the existence of a contraction mapping

$$\| \underbrace{\boldsymbol{r}_i^{L+1,K} - \boldsymbol{r}_i^{L+1}}_{\varpi_i^{L+1,K}} \| = \|\mathcal{G}(\boldsymbol{r}_i^{L+1,K-1}) - \mathcal{G}(\boldsymbol{r}_i^{L+1})\| \leq \eta^{L+1,K} \|\boldsymbol{r}_i^{L+1,K-1} - \boldsymbol{r}_i^{L+1}\|, \tag{C.4}$$

where, if $0 \leq \eta^{L+1,K} < 1$ for each iteration K, then $\varpi_i^{L+1,K} \rightarrow \mathbf{0}$ for any arbitrary starting value $\boldsymbol{r}_i^{L+1,K=0}$, as $K \rightarrow \infty$, which is a contraction condition that is sufficient, but not necessary, for convergence. The convergence of Eq. (C.1) is scaled by $\eta \propto \frac{(\phi \Delta t)^2}{m_i}$. Therefore, we see that the contraction constant of $\mathcal{G}$ is (a) directly dependent on the magnitude of the interaction forces ($\| \boldsymbol{\Psi} \|$), (b) inversely proportional to the masses m_i and (c) directly proportional to $(\Delta t)^2$. Thus, decreasing the time step size improves the convergence. *In order to maximize the time-step sizes (to decrease overall computing time) and still meet an error tolerance on the numerical solution's accuracy*, we build on an approach originally developed for continuum thermo-chemical multifield problems (Zohdi [52]), where one assumes: (1) $\eta^{L+1,K} \approx S(\Delta t)^p$, ($S$ is a constant) and (2) the error within an iteration behaves according to $(S(\Delta t)^p)^K \varpi^{L+1,0} = \varpi^{L+1,K}$, $K = 1, 2, \ldots$, where $\varpi^{L+1,0} = \boldsymbol{r}^{L+1,K=1} - \boldsymbol{r}^L$ is the initial norm of the iterative (relative) error and S is intrinsic to the system. For example, for second-order problems, due to the quadratic dependency on Δt, $p \approx 2$. The objective is to meet an error tolerance in exactly a preset (the analyst sets this) number of iterations. To this end, one writes $(S(\Delta t_{\text{tol}})^p)^{K_d} \varpi^{L+1,0} = TOL$, where TOL is a tolerance and where K_d is the number of desired iterations. If the error tolerance is not met in the desired number of iterations, the contraction constant $\eta^{L+1,K}$ is too large. Accordingly, one can solve for a new smaller step size, under the assumption that S is constant,

$$\Delta t_{\text{tol}} = \Delta t \left(\frac{(\frac{TOL}{\varpi^{L+1,0}})^{\frac{1}{pK_d}}}{(\frac{\varpi^{L+1,K}}{\varpi^{L+1,0}})^{\frac{1}{pK}}} \right) \stackrel{\text{def}}{=} \Delta t \Lambda_K . \tag{C.5}$$

The assumption that S is constant is not critical, since the time steps are to be recursively refined and unrefined throughout the simulation. Clearly, the expression in Eq. (C.5) can also be used for time step enlargement, if convergence is met in less than K_d iterations (typically chosen to be between five to ten iterations).

References

[1] C. Hull, Apparatus for Production of Three-Dimensional Objects by Stereolithography, 1984, U.S. Patent 4,575,330.

[2] Y. Huang, M.C. Leu, J. Mazumdar, A. Donmez, Additive manufacturing: current state, future potential, gaps and needs, and recommendation, J. Manuf. Sci. Eng. 137 (2015) 014001-1.

[3] J. Duran, Sands, Powders and Grains. An Introduction to the Physics of Granular Matter, Springer Verlag, 1997.

[4] T. Pöschel, T. Schwager, Computational Granular Dynamics, Springer Verlag, 2004.

[5] E. Oñate, S.R. Idelsohn, M.A. Celigueta, R. Rossi, Advances in the particle finite element method for the analysis of fluid-multibody interaction and bed erosion in free surface flows, Comput. Methods Appl. Mech. Engrg. 197 (19–20) (2008) 1777–1800.

[6] E. Oñate, M.A. Celigueta, S.R. Idelsohn, F. Salazar, B. Suárez, Possibilities of the particle finite element method for fluid-soil–structure interaction problems, Comput. Mech. 48 (2011) 307–318.

[7] E. Oñate, M.A. Celigueta, S. Latorre, G. Casas, R. Rossi, J. Rojek, Lagrangian analysis of multiscale particulate flows with the particle finite element method, Comput. Part. Mech. 1 (1) (2014) 85–102.

[8] J. Rojek, C. Labra, O. Su, E. Oñate, Comparative study of different discrete element models and evaluation of equivalent micromechanical parameters, Int. J. Solids Struct. 49 (2012) 1497–1517. http://dx.doi.org/10.1016/j.ijsolstr.2012.02.032.

[9] J. Rojek, Discrete element thermomechanical modeling of rock cutting with valuation of tool wear, Comput. Part. Mech. 1 (1) (2014) 71–84.

[10] J.M. Carbonell, E. Oñate, B. Suarez, Modeling of ground excavation with the particle finite element method, ASCE J. Eng. Mech. 136 (2010) 455–463.

[11] C. Labra, E. Oñate, High-density sphere packing for discrete element method simulations, Commun. Numer. Methods. Eng. 25 (7) (2009) 837–849.

[12] D. Mukherjee, T.I. Zohdi, Electromagnetic control of charged particulate spray systems - models for planning the spray gun operations, Computer-Aided Des. 46 (2014) 211–215.

[13] D. Mukherjee, Z. Zaky, T.I. Zohdi, A. Salama, S. Sun, Investigation of guided particle transport for noninvasive healing of damaged piping system using electro-magneto-mechanical methods, J. Soc. Pet. Eng. SPE 169639 (2015) 1–12.

[14] D. Mukherjee, T.I. Zohdi, A discrete element based simulation framework to investigate particulate spray deposition processes, J. Comput. Phys. 290 (2015) 298–317.

[15] D. Mukherjee, T.I. Zohdi, Computational modeling of the dynamics and interference effects of an erosive granular jet impacting a porous, compliant surface, Granular Matter 17 (2015) 231–252.

[16] T.I. Zohdi, Electromagnetic properties of multiphase dielectrics, in: A Primer on Modeling, Theory and Computation (Peer Reviewed), Springer-Verlag, 2012.

[17] O.C. Zienkiewicz, Coupled problems & their numerical solution, in: R.W. Lewis, P. Bettes, E. Hinton (Eds.), Numerical Methods in Coupled Systems, Wiley, Chichester, 1984, pp. 35–58.

[18] O.C. Zienkiewicz, D.K. Paul, A.H.C. Chan, Unconditionally stable staggered solution procedure for soil-pore fluid interaction problems, Internat. J. Numer. Methods Engrg. 26 (1988) 1039–1055.

[19] R.W. Lewis, B.A. Schrefler, L. Simoni, Coupling versus uncoupling in soil consolidation, Int. J. Numer. Anal. Methods Geomech. 15 (1992) 533–548.

[20] R.W. Lewis, B.A. Schrefler, The Finite Element Method in the Static & Dynamic Deformation & Consolidation of Porous Media, second ed., Wiley Press, 1998.
[21] K.C. Park, C.A. Felippa, Partitioned analysis of coupled systems, in: T. Belytschko, T.J.R. Hughes (Eds.), Computational Methods for Transient Analysis, 1983.
[22] C. Farhat, M. Lesoinne, N. Maman, Mixed explicit/implicit time integration of coupled aeroelastic problems: three-field formulation, geometric conservation and distributed solution, Internat. J. Numer. Methods Fluids 21 (1995) 807–835.
[23] C. Farhat, M. Lesoinne, Two efficient staggered procedures for the serial and parallel solution of three-dimensional nonlinear transient aeroelastic problems, Comput. Methods Appl. Mech. Engrg. 182 (2000) 499–516.
[24] C. Farhat, G. van der Zee, P. Geuzaine, Provably second-order time-accurate loosely-coupled solution algorithms for transient nonlinear computational aeroelasticity, Comput. Methods Appl. Mech. Engrg. 195 (2006) 1973–2001.
[25] S. Piperno, Explicit/implicit fluid/structure staggered procedures with a structural predictor & fluid subcycling for 2d inviscid aeroelastic simulations, Internat. J. Numer. Methods Fluids 25 (1997) 1207–1226.
[26] S. Piperno, C. Farhat, B. Larrouturou, Partitioned procedures for the transient solution of coupled aeroelastic problems - Part I: Model problem, theory, and two-dimensional application, Comput. Methods Appl. Mech. Engrg. 124 (1–2) (1995) 79–112.
[27] S. Piperno, C. Farhat, Partitioned procedures for the transient solution of coupled aeroelastic problems - Part II: Energy transfer analysis and three-dimensional applications, Comput. Methods Appl. Mech. Engrg. 190 (2001) 3147–3170.
[28] G. Michopoulos, C. Farhat, J. Fish, Survey on modeling and simulation of multiphysics systems, J. Comput. Inf. Sci. Eng. 5 (3) (2005) 198–213.
[29] M. Lesoinne, C. Farhat, Free staggered algorithm for nonlinear transient aeroelastic problems, AIAA J. 36 (9) (1998) 1754–1756.
[30] P. Le Tallec, J. Mouro, Fluid structure interaction with large structural displacements, Comput. Methods Appl. Mech. Engrg. 190 (24–25) (2001) 3039–3067.
[31] B. Widom, Random sequential addition of hard spheres to a volume, J. Chem. Phys. 44 (1966) 3888–3894.
[32] S. Torquato, Random Heterogeneous Materials: Microstructure and Macroscopic Properties, Springer-Verlag, New York, 2002.
[33] A. Kansaal, S. Torquato, F. Stillinger, Diversity of order & densities in jammed hard-particle packings, Phys. Rev. E 66 (2002) 041109.
[34] D.T. Papageorgiou, On the breakup of viscous liquid threads, Phys. Fluids 7 (7) (1995) 1521–1529.
[35] J. Eggers, Nonlinear dynamics and breakup of free-surface flows, Rev. Modern Phys. 69 (3) (1997) 865.
[36] T.I. Zohdi, Computational modeling of electrically-driven deposition of ionized polydisperse particulate powder mixtures in advanced manufacturing processes, J. Comput. Phys. (2017). http://dx.doi.org/10.1016/j.jcp.2017.03.044.
[37] B. Avci, P. Wriggers, A DEM-FEM coupling approach for the direct numerical simulation of 3D particulate flows, J. Appl. Mech. 79 (2012) 010901-(1-7).
[38] A. Leonardi, F.K. Wittel, M. Mendoza, H.J. Herrmann, Coupled DEM-LBM method for the free-surface simulation of heterogeneous suspensions, Comput. Part. Mech. 1 (1) (2014) 3–13.
[39] D.S. Bolintineanu, G.S. Grest, J.B. Lechman, F. Pierce, S.J. Plimpton, P.R. Schunk, Particle dynamics modeling methods for colloid suspensions, Comput. Part. Mech. 1 (3) (2014) 321–356.
[40] V.V. Jikov, S.M. Kozlov, O.A. Olenik, Homogenization of Differential Operators and Integral Functionals, Springer-Verlag, 1994.
[41] Z. Hashin, Analysis of composite materials: a survey, ASME J. Appl. Mech. 50 (1983) 481–505.
[42] T. Mura, Micromechanics of Defects in Solids, second ed., Kluwer Academic Publishers, 1993.
[43] K.Z. Markov, Elementary micromechanics of heterogeneous media, in: K.Z. Markov, L. Preziozi (Eds.), Heterogeneous Media: Micromechanics Modeling Methods and Simulations, Birkhauser, Boston, 2000, pp. 1–162.
[44] S. Ghosh, Micromechanical Analysis and Multi-Scale Modeling using the Voronoi Cell Finite Element Method, CRC Press/Taylor & Francis, 2011.
[45] S. Ghosh, D. Dimiduk, Computational Methods for Microstructure-Property Relations, Springer, NY, 2011.
[46] K. Matous, M. Geers, V.G. Kouznetsova, A. Gillman, A review of predictive nonlinear theories for multiscale modeling of heterogeneous materials, Archives Comput. Methods Engrg. 24 (1) (2017) 89–113.
[47] T.I. Zohdi, D.A. Dornfeld, Future Synergy between Computational Mechanics and Advanced Additive Manufacturing. US National Academies Report, 2015: http://sites.nationalacademies.org/cs/groups/pgasite/documents/webpage/pga_166813.pdf.
[48] K. Johnson, Contact Mechanics, Cambridge University Press, 1985.
[49] P. Wriggers, Computational Contact Mechanics, John-Wiley, 2002.
[50] P. Wriggers, Nonlinear Finite Element Analysis, Springer, 2008.
[51] C.Y. Chow, An Introduction to Computational Fluid Dynamics, Wiley, New York, 1980.
[52] T.I. Zohdi, An adaptive-recursive staggering strategy for simulating multifield coupled processes in microheterogeneous solids, Internat. J. Numer. Methods Engrg. 53 (2002) 1511–1532.
[53] P. Martin, HandBook of Deposition Technologies for Films and Coatings, third ed., Elsevier, 2009.
[54] P. Martin, Introduction to Surface Engineering and Functionally Engineered Materials, Scrivener and Elsevier, 2011.
[55] S. Choi, I. Park, Z. Hao, H.Y. Holman, A.P. Pisano, T.I. Zohdi, Ultra-fast self-assembly of micro-scale particles by open channel flow, Langmuir 26 (7) (2010) 4661–4667.
[56] S. Choi, S. Stassi, A.P. Pisano, T.I. Zohdi, Coffee-Ring Effect-Based Three Dimensional Patterning of Micro, Nanoparticle Assembly with a Single Droplet, Langmuir 26 (14) (2010) 11690–11698.
[57] S. Choi, A. Jamshidi, T.J. Seok, T.I. Zohdi, M.C. Wu, A.P. Pisano, Fast, high-throughput creation of size-tunable micro, nanoparticle clusters via evaporative self-assembly in picoliter-scale droplets of particle suspension, Langmuir 28 (6) (2012) 3102–3111.
[58] S. Choi, A.P. Pisano, T.I. Zohdi, An analysis of evaporative self-assembly of micro particles in printed picoliter suspension droplets, J. Thin Solid Films 537 (30) (2013) 180–189.

[59] M. Demko, S. Choi, T.I. Zohdi, A.P. Pisano, High resolution patterning of nanoparticles by evaporative self-assembly enabled by in-situ creation and mechanical lift-off of a polymer template, Appl. Phys. Lett. 99 (2012) 253102–1–253102–3.
[60] I. Sevostianov, M. Kachanov, Modeling of the anisotropic elastic properties of plasma-sprayed coatings in relation to their microstructure", with I. Sevostianov, Acta Mater. 48 (6) (2000) 1361–1370.
[61] I. Sevostianov, M. Kachanov, Thermal conductivity of plasma sprayed coatings in relation to their microstructure, with I Sevostianov, J. Therm. Spray Technol. 9 (4) (2001) 478–482.
[62] I. Sevostianov, M. Kachanov, Plasma-sprayed ceramic coatings: anisotropic elastic and conductive properties in relation to the microstructure; cross-property correlations", with I. Sevostianov, Mater. Sci. Eng. A 297 (2001) 235–243.
[63] G. Qian, T. Nakamura, C.C. Berndt, Effects of thermal gradient and residual stresses on thermal barrier coating fracture, Mech. Mater. 27 (1998) 91–110.
[64] G. Dwivedi, T. Wentz, S. Sampath, T. Nakamura, Assessing process and coating reliability through monitoring of process and design relevant coating properties, J. Thermal Spray Technol. 19 (2010) 695–712.
[65] Y. Liu, T. Nakamura, G. Dwivedi, A. Valarezo, S. Sampath, Anelastic behavior of plasma sprayed zirconia coatings, J. Am. Ceram. Soc. 91 (2008) 4036–4043.
[66] Y. Liu, T. Nakamura, V. Srinivasan, A. Vaidya, A. Gouldstone, S. Sampath, Nonlinear elastic properties of plasma sprayed zirconia coatings and associated relationships to processing conditions, Acta Mater. 55 (2007) 4667–4678.
[67] T. Nakamura, Y. Liu, Determination of nonlinear properties of thermal sprayed ceramic coatings via inverse analysis, Int. J. Solids Struct. 44 (2007) 1990–2009.
[68] T. Nakamura, G. Qian, C.C. Berndt, Effects of pores on mechanical properties of plasma sprayed ceramic coatings, J. Am. Ceram. Soc. 83 (2000) 578–584.
[69] D. Gamota, P. Brazis, K. Kalyanasundaram, J. Zhang, Printed Organic and Molecular Electronics, Kluwer Academic Publishers, New York, 2004.
[70] H. Nakanishi, K.J.M. Bishop, B. Kowalczyk, A. Nitzan, E.A. Weiss, K.V. Tretiakov, M.M. Apodaca, R. Klajn, J.F. Stoddart, B.A. Grzybowski, Photoconductance and inverse photoconductance in thin films of functionalized metal nanoparticles, Nature 460 (2009) 371–375.
[71] S.B. Fuller, E.J. Wilhelm, J.M. Jacobson, Ink-jet printed nanoparticle microelectromechanical systems, J. Microelectromech. Syst. 11 (2002) 54–60.
[72] S.R. Samarasinghe, I. Pastoriza-Santos, M.J. Edirisinghe, M.J. Reece, L.M. Liz-Marzan, Printing gold nanoparticles with an electrohydrodynamic direct write device, Gold Bull. 39 (2006) 48–53.
[73] Z. Ahmad, M. Rasekh, M. Edirisinghe, Electrohydrodynamic direct writing of biomedical polymers and composites, Macromolecular Mater. Eng. 295 (2010) 315–319.
[74] H. Sirringhaus, T. Kawase, R.H. Friend, T. Shimoda, M. Inbasekaran, W. Wu, E.P. Woo, High-resolution inkjet printing of all-polymer transistor circuits, Science 290 (2000) 2123–2126.
[75] J.Z. Wang, Z.H. Zheng, H.W. Li, W.T.S. Huck, H. Sirringhaus, Dewetting of conducting polymer inkjet droplets on patterned surfaces, Nat. Mater. 3 (2004) 171–176.
[76] D. Huang, F. Liao, S. Molesa, D. Redinger, V. Subramanian, Plastic-compatible low-resistance printable gold nanoparticle conductors for flexible electronics, J. Electrochem. Soc. 150 (7) (2003) G412–417.
[77] M.T. Demko, J.C. Cheng, A.P. Pisano, High-resolution direct patterning of gold nanoparticles by the microfluidic molding process, Langmuir (2010) 412–417.
[78] T.I. Zohdi, Simulation of coupled microscale multiphysical-fields in particulate-doped dielectrics with staggered adaptive FDTD, Comput. Methods Appl. Mech. Eng. 199 (2010) 79–101.
[79] T.I. Zohdi, Rapid simulation of laser processing of discrete particulate materials, Arch. Comput. Methods Eng. 20 (2013) 309–325.
[80] T.I. Zohdi, Additive particle deposition and selective laser processing-a computational manufacturing framework, Comput. Mech. 54 (2014) 171–191.
[81] T.I. Zohdi, Modeling and simulation of cooling-induced residual stresses in heated particulate mixture depositions, Comput. Mech. 56 (2015) 613–630.
[82] T.I. Zohdi, Modeling and simulation of laser processing of particulate-functionalized materials, Arch. Comput. Methods Eng. (2015) 1–25. http://dx.doi.org/10.1007/s11831-015-9160-1.
[83] T.I. Zohdi, P. Wriggers, Introduction to Computational Micromechanics, Springer-Verlag, 2008 Second Reprinting.
[84] J.D. Jackson, Classical Electrodynamics, third ed., Wiley, 1998.
[85] T.I. Zohdi, Modeling and direct simulation of near-field granular flows, Int. J. Solids Struct. 42/2 (2004) 539–564.
[86] T.I. Zohdi, Charge-induced clustering in multifield particulate flow, Internat. J. Numer. Methods Engrg. 62 (7) (2005) 870–898.
[87] T.I. Zohdi, Computation of strongly coupled multifield interaction in particle-fluid systems, Comput. Methods Appl. Mech. Engrg. 196 (2007) 3927–3950.
[88] T.I. Zohdi, Numerical simulation of charged particulate cluster-droplet impact on electrified surfaces, J. Comput. Phys. 233 (2013) 509–526.
[89] T.I. Zohdi, A direct particle-based computational framework for electrically-enhanced thermo-mechanical sintering of powdered materials, Math. Mech. Solids 19 (1) (2014) 93–113.
[90] T.I. Zohdi, Embedded electromagnetically sensitive particle motion in functionalized fluids, Comput. Part. Mech. 1 (2014) 27–45.
[91] M. Frenklach, C.S. Carmer, Molecular dynamics using combined quantum & empirical forces: application to surface reactions, Adv. Class. Trajectory Methods 4 (1999) 27–63.
[92] J.M. Haile, Molecular Dynamics Simulations: Elementary Methods, Wiley, 1992.

[93] W.L. Hase, Molecular Dynamics of Clusters, Surfaces, Liquids, & Interfaces. Advances in Classical Trajectory Methods, Vol 4., JAI Press, 1999.
[94] T. Schlick, Molecular Modeling & Simulation. An Interdisciplinary Guide, Springer-Verlag, New York, 2000.
[95] D.C. Rapaport, The Art of Molecular Dynamics Simulation, Cambridge University Press, 1995.
[96] E.A. Moelwyn-Hughes, Physical Chemistry, Pergamon, 1961.
[97] J. Tersoff, Empirical interatomic potential for carbon, with applications to amorphous carbon, Phys. Rev. Lett. 61 (1988) 2879–2882.
[98] F.H. Stillinger, T.A. Weber, Computer simulation of local order in condensed phases of silicon, Phys. Rev. B 31 (1985) 5262–5271.
[99] Richard P. Feynman, Robert B. Leighton, Matthew Sands, The Feynman Lectures on Physics, Vol. 2, ISBN: 0-8053-9045-6, 2006.
[100] C. Cullity, D. Graham, Introduction to Magnetic Materials, second ed., Wiley-IEEE Press, ISBN: 0-471-47741-9, 2008, p. 103.
[101] Timothy H. Boyer, The force on a magnetic dipole, Amer. J. Phys. 56 (8) (1988) 688–692. http://dx.doi.org/10.1119/1.15501. Bibcode:1988AmJPh.56688B.
[102] A. Donev, I. Cisse, D. Sachs, E.A. Variano, F. Stillinger, R. Connelly, S. Torquato, P. Chaikin, Improving the density of jammed disordered packings using ellipsoids, Science 303 (2004) 990–993.
[103] A. Donev, F.H. Stillinger, P.M. Chaikin, S. Torquato, Unusually dense crystal ellipsoid packings, Phys. Rev. Lett. 92 (2004) 255506.
[104] A. Donev, S. Torquato, F. Stillinger, Neighbor list collision-driven molecular dynamics simulation for nonspherical hard particles-I. Algorithmic details, J. Comput. Phys. 202 (2005) 737.
[105] A. Donev, S. Torquato, F. Stillinger, Neighbor list collision-driven molecular dynamics simulation for nonspherical hard particles-II. Application to ellipses and ellipsoids, J. Comput. Phys. 202 (2005) 765.
[106] A. Donev, S. Torquato, F.H. Stillinger, Pair correlation function characteristics of nearly jammed disordered and ordered hard-sphere packings, Phys. Rev. E 71 (2005) 011105.
[107] B.A. Ridley, B. Nivi, J.M. Jacobson, All-inorganic field effect transistors fabricated by printing, Science 286 (1999) 746–749.
[108] C. Wellmann, C. Lillie, P. Wriggers, A contact detection algorithm for superellipsoids based on the common-normal concept, Eng. Comput. 25 (2008) 432–442.
[109] C. Wellmann, C. Lillie, P. Wriggers, Homogenization of granular material modeled by a three-dimensional discrete element method, Comput. Geotech. 35 (2008) 394–405.
[110] C. Wellmann, C. Lillie, P. Wriggers, Comparison of the macroscopic behavior of granular materials modeled by different constitutive equations on the microscale, Finite Elem. Anal. Des. 44 (2008) 259–271.
[111] C. Wellmann, P. Wriggers, in: E.E Oñate, D.R.J. Owen (Eds.), Homogenization of Granular Material Modeled by a 3D DEM, Particle-Based Methods: Fundamentals and Applications, 2011, pp. 211–231.
[112] C. Wellmann, P. Wriggers, A two-scale model of granular materials, Comput. Methods Appl. Mech. Engrg. 205–208 (2012) 46–58.
[113] T.I. Zohdi, Modeling and simulation of a class of coupled thermo-chemo-mechanical processes in multiphase solids, Comput. Methods Appl. Mech. Engrg. 193/6-8 (2004) 679–699.
[114] T.I. Zohdi, A computational framework for agglomeration in thermo-chemically reacting granular flows, Proc. Roy. Soc. 460 (2052) (2004) 3421–3445.
[115] T.I. Zohdi, On the computation of the coupled thermo-electromagnetic response of continua with particulate microstructure, Internat. J. Numer. Methods Engrg. 76 (2008) 1250–1279.
[116] T.I. Zohdi, On the dynamics of charged electromagnetic particulate jets, Arch. Comput. Methods Eng. 17 (2) (2010) 109–135.
[117] T.I. Zohdi, Modeling and efficient simulation of the deposition of particulate flows onto compliant substrates, Internat. J. Eng. Sci. 99 (2015) 74–91. http://dx.doi.org/10.1016/j.ijengsci.2015.10.012.